Chapter 5
Dynamic Mass Density and Acoustic Metamaterials

Jun Mei, Guancong Ma, Min Yang, Jason Yang, and Ping Sheng

Abstract Elastic and electromagnetic waves are two types of classical waves that, though very different, nevertheless display many analogous features. In particular, for the acoustic waves, there can be a correspondence between the two material parameters of the acoustic wave equation, the mass density and bulk modulus, with the dielectric constant and magnetic permeability of the Maxwell equations. We show that the classical mass density, a quantity that is often regarded as positive definite in value, can display complex finite-frequency characteristics for a composite that comprises local resonators, thereby leading to acoustic metamaterials in exact analogy with the electromagnetic metamaterials. In particular, we demonstrate that through the anti-resonance mechanism, a locally resonant sonic material is capable of totally reflecting low-frequency sound at a frequency where the effective dynamic mass density can approach positive and negative infinities. The condition that leads to the anti-resonance thereby offers a physical explanation of the metamaterial characteristics for both the membrane resonator and the 3D locally resonant sonic materials. Besides the metamaterials arising from the dynamic mass density behavior at finite frequencies, we also present a review of other relevant types of acoustic metamaterials. At the zero-frequency limit, i.e., in the absence of resonances, the dynamic mass density for the fluid–solid composites is shown to still differ significantly from the usual volume-averaged expression. We offer both a physical explanation and a rigorous mathematical derivation of the dynamic mass density in this case.

J. Mei • G. Ma • M. Yang • J. Yang • P. Sheng (✉)
Department of Physics, The Hong Kong University of Science and Technology, Clear Water Bay, Kowloon, Hong Kong, China
e-mail: sheng@ust.hk

P.A. Deymier (ed.), *Acoustic Metamaterials and Phononic Crystals*,
Springer Series in Solid-State Sciences 173, DOI 10.1007/978-3-642-31232-8_5,
© Springer-Verlag Berlin Heidelberg 2013

5.1 Introduction

The novel characteristics of metamaterials represent an emergent phenomenon in which the basic mechanism of resonances, when considered in aggregate, can give rise to material properties that are outside the realm provided by Nature. In the case of acoustic metamaterials, the novel characteristics directly arise from the finite-frequency behavior of the two relevant material parameters—the mass density and bulk modulus. The focus of this chapter is on the dynamic mass density and its related metamaterial characteristics. For completeness, a brief review of other types of acoustic metamaterials is also presented.

It is well known that in the quantum mechanical band theory of solids, the effective mass of an electron can change sign depending on its energy within an energy band. However, as this is attributed to the electron's wave character, the classical mass density is usually regarded as a positive-definite quantity since the quantum mechanical effects are absent. In particular, for a two-component composite, the effective mass density is usually given by the volume-averaged value:

$$\rho_{\text{eff}} = fD_1 + (1-f)D_2, \tag{5.1}$$

where $D_{1(2)}$ denotes the mass density of the 1st (2nd) component, and f is the volume fraction of component 1. We denote the static mass density (5.1) ρ_{eff}.

An implicit assumption underlying the validity of the static mass density expression is that in the presence of wave motion, the two components of the composite *move in unison*. However, this assumption is not always true. For a composite comprising many identical local resonators embedded in a matrix material, if the local resonators' masses move out of phase with the matrix displacement (as when the wave frequency ω exceeds the resonance frequency of the resonators), then we have a case in which the matrix and the resonators' masses display *relative motion*. If, in addition, we assume that the local resonators occupy a significant volume fraction, then it is clear that within a particular frequency range, the overall effective mass density can appear to be negative [1–6]. This fact can be simply illustrated in a one-dimensional (1D) model [7, 8], where n cylindrical cavities of length d are embedded in a bar of rigid material. Within each cavity, a sphere of mass m is attached to the cavity wall by two identical springs with elastic constant K. An external force F acts on the rigid bar, which has a static mass M_0, as shown in Fig. 5.1.

For the first resonator, the displacements of the sphere and the right wall are denoted by u and U, respectively (Fig. 5.1). By assuming that $-f_1$ and $-f_2$ are the forces on the sphere exerted by the left and right springs, respectively, with f_2 along the same direction as F, and f_1 the opposite, then Hook's law tells us that $-f_1 + f_2 = -2K(U-u)$. From Newton's second law, we have $f_1 - f_2 = (-i\omega)^2 mu$. From these two relations, we obtain $u = \frac{2K}{2K - m\omega^2}U$. Applying Newton's second law to the rigid bar, we have $F + n(f_2 - f_1) = (-i\omega)^2 M_0 U$. Hence $F = (-i\omega)^2 [M_0 U + nmu] = (-i\omega)^2 (D_{\text{eff}} V) U$. Here the effective *dynamic mass density* D_{eff} is defined as $F/(-\omega^2 U)$:

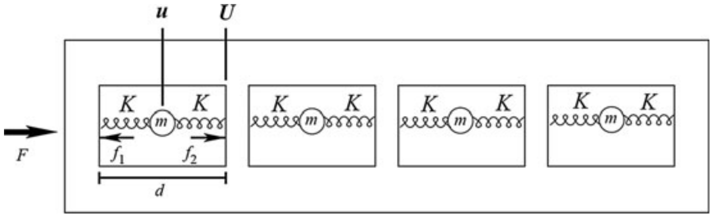

Fig. 5.1 A one-dimensional acoustic metamaterial composed of a series of local resonators embedded in a rigid bar. Here the directions of f_1 and f_2 are shown as that on the left and right walls of the cavity, respectively. Adapted from [7]

$$D_{\mathrm{eff}}V = M_0 + nm\frac{u}{U} = M_0 + \frac{nm}{1-(\omega^2/\omega_0^2)}, \tag{5.2}$$

where $\omega_0^2 = 2K/m$ and V denotes the total volume of the system. Thus *negative* dynamic mass is possible at finite frequencies (when ω^2 is in the range of ω_0^2), and this phenomenon enables the realization of acoustic metamaterials. Equation (5.2) is also informative in showing that the dynamic mass density is generally defined as the averaged force density f divided by the averaged acceleration a, i.e.,

$$D_{\mathrm{eff}} = \langle f\rangle/\langle a\rangle, \tag{5.3}$$

where $\langle\rangle$ denotes averaging over interfaces with the external region of the observer. Obviously, this is precisely how (5.2) is obtained. The above simple example serves to illustrate the point that the dynamic mass density, in the presence of relative motion between the components, can differ from the volume-averaged static mass density. In more realistic models in which the matrix is an elastic medium, it will be shown below that the dynamic mass density's resonance-like behavior is directly associated with the *anti-resonance(s)* of the system.

In the limit of $\omega \to 0$ so that resonances can be excluded, the volume-averaged mass density holds true for most composites. However, the fluid–solid composites constitute an important exception. A well-known example is the fourth sound of liquid helium 4 in a porous medium [9], which arises from the *relative* motion between the liquid helium 4 and the solid frame—even at the low-frequency limit. More generally, it is well known that for a fluid–solid composite, there is a viscous boundary layer thickness $\ell_{\mathrm{vis}} = \sqrt{\eta/\rho_{\mathrm{f}}\omega}$ at the fluid–solid interface, where η denotes the fluid viscosity and ρ_{f} the fluid density. It is clear from the definition of ℓ_{vis} that the $\eta \to 0$ limit cannot be interchanged with the $\omega \to 0$ limit since in the former case $\ell_{\mathrm{vis}} \to 0$ whereas in the latter case we have $\ell_{\mathrm{vis}} \to \infty$. Thus the Biot slow wave, predicted as a second longitudinal wave in a fluid–solid composite [10] and eventually experimentally verified [11], may be viewed as a "fourth sound" for the viscous fluid, valid when the pore size ℓ of the porous medium is larger than ℓ_{vis} [12]. Thus the dynamic mass density of a fluid–solid composite is what governs the wave propagation when the dimensionless ratio $\sqrt{\eta/\rho_{\mathrm{f}}\omega}/\ell << 1$.

In what follows, we describe in Sect. 5.2 the initial realization of acoustic metamaterials based on the concept of local resonators and their special characteristics. In particular, it is shown that such metamaterials can break the mass density law, which governs air-borne sound attenuation through a solid wall. This is followed by the presentation of the membrane-type metamaterials in Sect. 5.3 that may be regarded as the two-dimensional (2D) version of resonant sonic materials. The unifying characteristic of the anti-resonance and negative dynamic mass density is emphasized in both Sects. 5.2 and 5.3. In Sect. 5.4, we give a brief review of other types of acoustic metamaterials that have since been realized. Section 5.5 is devoted to the dynamic mass density in the low-frequency limit (for the fluid–solid composites), prefaced by a short review of the multiple-scattering theory (MST). We conclude in Sect. 5.6 with a brief summary and some remarks on the prospects and challenges.

5.2 Locally Resonant Sonic Materials: A Metamaterial Based on the Dynamic Mass Density Effects

In Fig. 5.2a we show a cross-sectional photo image of the basic unit for the locally resonant sonic material [1]. It comprises a metallic sphere 5 mm in radius coated by a layer of silicone rubber. Figure 5.2b is a picture showing a cube assembled from these basic units with epoxy, in a simple cubic structure with a lattice constant of 1.55 cm. It is clear that the metallic sphere of the basic unit acts as a heavy mass, with silicone rubber as the weak spring. Hence there must be a low-frequency resonance. Moreover, the resonance is local in character, to be distinguished from the structural resonances that are common to any mechanical object. Figure 5.2c, d show the transmission characteristics and band structure of the crystal shown in Fig. 5.2b, respectively. It is noted that there is a deep transmission dip at 380 Hz, followed by a transmission maximum at 610 Hz. This pattern is repeated at 1,340 Hz and 1,580 Hz. Here the solid line is the theory prediction calculated from the MST, and the solid circles are the measured data. They show good agreement. In Fig. 5.2d, the calculated band structure is shown. The flat band edges, at 380 Hz and 1,340 Hz, are characteristic of local (anti-)resonances that are very weakly coupled to each other.

It is seen that the structure shown in Fig. 5.2b has a complete bandgap between 380 Hz and 610 Hz. In contrast to phononic crystals where the relevant wavelength corresponding to the primary bandgap frequency must be comparable to the lattice constant, here the wavelength (in epoxy) at 380 Hz is ~300 times the lattice constant. That is, the locally resonant sonic materials can open phononic gaps at frequencies that are much lower than that derived from considerations of their structural length scales. In fact, since the effect is due to local resonances, and these resonances depend only on the rubber's elastic constants and metal sphere's mass, the bandgap frequency should be totally decoupled from structural considerations.

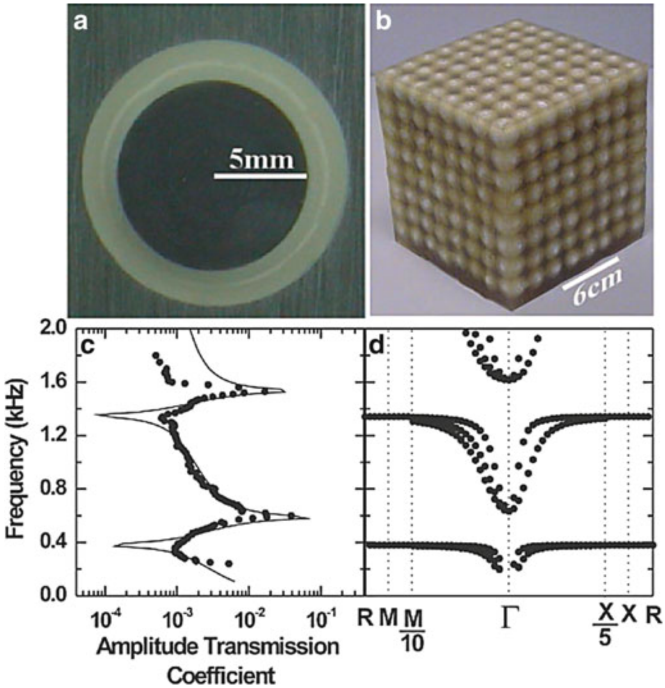

Fig. 5.2 (**a**) Cross section of a coated sphere that forms the basic structure unit (**b**) for an 8 × 8 ×8 sonic crystal. (**c**) Calculated (*solid line*) and measured (*circles*) amplitude transmission coefficients along the [100] direction are plotted as a function of frequency. The calculation is for a four-layer slab of simple cubic arrangement of coated spheres, periodic parallel to the slab. The observed transmission characteristics correspond well with the calculated band structure (**d**), from 200 to 2,000 Hz, of a simple cubic structure of coated spheres. Figure adapted from [1]

The fact that the locally resonant sonic materials can have bandgaps may be simply explained by using analogy with the tight binding approach for the electronic structure calculations, in which the starting point is the discrete electronic energy levels in individual atoms. Our local resonances also have a discrete spectrum. When the atoms interact with each other (through the hopping matrix element in the tight binding formulation), the discrete energy levels broaden into energy bands. If the interaction is weak, the bands may not completely overlap and what remain are exactly the bandgaps. Moreover, the band edges are usually flat just as what we see in Fig. 5.2d. From this analogy, it is plausible that since periodicity plays only an implicit role in the tight binding approach, it may not be a necessary requirement for the creation of bandgaps. Hence it was shown by Weaire [13] that in tetrahedrally bonded system (such as the amorphous silicon), the existence of bandgaps indeed does not require long-range periodic order. This is another aspect that differs from phononic crystals, in which the bandgap is the result of Bragg scattering.

Below we present the novel functionality of the locally resonant sonic material together with its relevant physics. It will be seen that the dynamic mass density behavior of the system naturally emerges as the dominant cause of its special characteristics.

5.2.1 Metamaterial Functionality

In Fig. 5.2c, it is seen that at 380 Hz, the locally resonant sonic material can have a sharp minimum in transmission. In order to appreciate the significance of this phenomenon, it is necessary to first review the law of acoustic attenuation by a solid wall, usually denoted the *mass density law*.

Consider a sound wave in air with angular frequency ω impinging normally on a solid wall of thickness d, mass density ρ_2 and bulk modulus κ_2. Sound transmission amplitude is given by

$$T = \frac{4v\exp(ik_2 d)}{(1+v)^2 - (1-v)^2\exp(2ik_2 d)}, \tag{5.4}$$

where $k_2 = \omega/\sqrt{\kappa_2/\rho_2}$ is the wavevector in solid and $v = \sqrt{\kappa_2\rho_2/\kappa_1\rho_1}$ is the solid–air impedance ratio, with κ_1 and ρ_1 denoting the bulk modulus and mass density of air, respectively. For solid walls that are less than a meter in thickness, which is usually the case, we have $k_2 d \ll 1$ and $v \gg 1$ for frequencies less than 1 kHz. In that limit, an accurate approximation to (5.4) is given by

$$T \cong i\frac{2\sqrt{\rho_1\kappa_1}}{\omega\rho_2 d}. \tag{5.5}$$

It is seen that the bulk modulus of the wall does not appear in (5.5). That is, to a high degree of accuracy, the sound attenuation through a solid wall is independent of whether the wall is rigid or soft. Only the wall's mass per unit area ($\rho_2 d$) matters. That is why (5.5) is called the mass density law. But perhaps the most important aspect of (5.5) is that T is inversely proportional to the sound frequency. Hence low-frequency sound is inherently difficult to attenuate. This is the reason why low-frequency noise is such a pernicious source of urban environmental pollution.

In Fig. 5.3, we plot the measured amplitude transmission coefficient (solid circles with the connecting solid line) for a 2.1-cm slab of composite material containing 48 vol% of *randomly dispersed* coated metal spheres (same as the one whose cross-sectional picture is shown in Fig. 5.2a) in an epoxy matrix. As a reference, the measured amplitude transmission coefficient through a 2.1-cm slab of epoxy is also plotted (open squares connected by thin solid line). The *dashed* and *dot-dashed lines*, respectively, show the calculated transmission amplitudes of a 2.1-cm epoxy slab and a 2.1-cm homogeneous slab of the same density as that of the

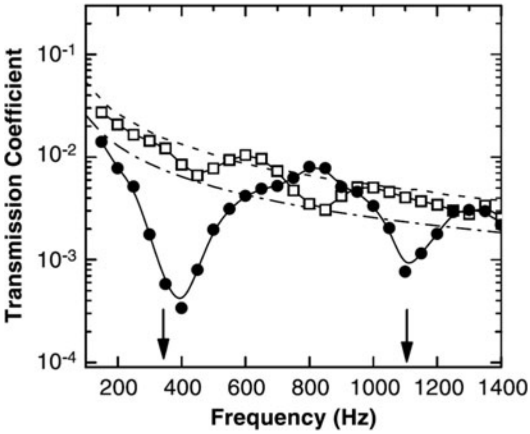

Fig. 5.3 Measured amplitude transmission (solid circles; the solid line is a guide to the eye) through a 2.1-cm slab of composite material containing 48 vol% of randomly dispersed coated lead spheres in an epoxy matrix. As a reference, the measured amplitude transmission through a 2.1-cm slab of epoxy is also plotted (*open squares* connected by a *thin solid line*). The dashed and dot-dashed lines, respectively, show the calculated transmission amplitudes of a 2.1-cm epoxy slab and a 2.1-cm homogeneous slab of the same density as that of the composite material containing the coated spheres. Adapted from [1]

composite material containing the coated spheres. The arrows indicate the dip frequency positions predicted by the multiple-scattering calculation for a monolayer of hexagonally arranged coated spheres in an epoxy matrix.

In Fig. 5.3, the comparison between the measured results for the composite slab and the mass density predictions shows clearly that the locally resonant sonic materials can break the mass density law at particular low-frequency regimes, thereby exhibiting acoustic metamaterial characteristics.

5.2.2 *Theoretical Understanding*

In order to gain an understanding of the metamaterial functionality, we have performed finite-element simulations by using the COMSOL Multiphysics. In the simulations, the mass density, Young's modulus, and Poisson's ratio for the lead sphere are 11.6×10^3kg/m^3, 4.08×10^{10}Pa, and 0.37, respectively. The mass density, Young's modulus, and Poisson's ratio for the silicone rubber are 1.3×10^3 kg/m^3, 1.18×10^5Pa, and 0.469, respectively. Corresponding parameters for epoxy are 1.18×10^3kg/m^3, 4.35×10^9Pa, and 0.368, respectively. Standard values for air, i.e., $\rho = 1.23\,\text{kg/m}^3$, ambient pressure of 1 atm, and speed of sound in air of $c = 340\,\text{m/s}$, were used. Two types of simulations were performed.

We first calculate the spectrum of transmission coefficients for a plane wave normally incident onto one unit cell along the z-direction. Periodic boundary conditions along the x- and y-directions were used. Radiation boundary conditions

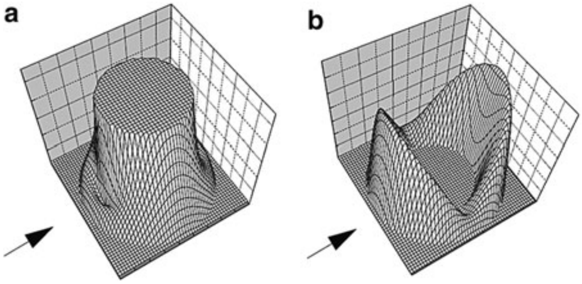

Fig. 5.4 Calculated displacement configurations around the first (**a**) and second (**b**) peak frequencies. The displacement show is for a cross section through the center of one coated sphere, located at the front surface. The *arrows* indicate the direction of the incident wave. Adapted from [1]

were used at the input and output planes of the air domain in the simulations. Two transmission peaks, with frequencies at 606 Hz and 1,576 Hz, were found. We also found two transmission dips, at 374 and 1,339 Hz.

We have also calculated the eigenmodes for one unit cell. Many eigenmodes were found. Out of these, we select the ones that are symmetric with respect to both the x- and y-directions, since otherwise the modes would not couple to the normally incident plane wave. The resulting triply degenerate eigenfrequencies are located at 606 and 1,571 Hz, respectively. They are seen to be *almost identical with the frequencies of the transmission peaks*.

In Fig. 5.4a, we show the calculated displacement configurations around the first peak frequency, where the lead sphere is seen to move as a whole along the direction of wave propagation. Around the second peak, the maximum displacement occurs inside the silicone rubber, as shown in Fig. 5.4b. In Fig. 5.5, we show the calculated strain tensor components ε_{xz} and ε_{yz} at the first and second dip frequencies, respectively. It can be seen that strains occur at the lead–rubber and/or the rubber–epoxy interfaces, which in fact can also be inferred from the displacement configurations as shown in Fig. 5.4. Below we show that the *dip frequencies correspond to anti-resonances* where the dynamic mass density displays a resonance-like behavior.

Figure 5.6 displays the calculated dynamic mass density D_{eff} for one unit cell of the locally resonant sonic material. Around 370 and 1,340 Hz, i.e., the transmission dip frequencies, the dynamic mass density $D_{\text{eff}} = \langle \nabla \cdot \sigma \rangle_z / \langle a_z \rangle$ clearly displays a resonance-like behavior. Thus the transmission peaks correspond with the eigenfrequencies, and the dips in the transmission are associated with anti-resonances at which we have a dynamic mass density resonance profile. In particular, it is shown below that at the anti-resonance frequencies, the average normal displacement of the unit cell surface (in the matrix material) vanishes, hence $\langle a_z \rangle = -\omega^2 \langle u_z \rangle$ goes through a zero and therefore it is easy to see that D_{eff} acquires a resonance-like behavior, with a diverging magnitude at the anti-resonance frequency. In a sense, the mass density law seems to recover its validity–but only if its value replaces the static mass density.

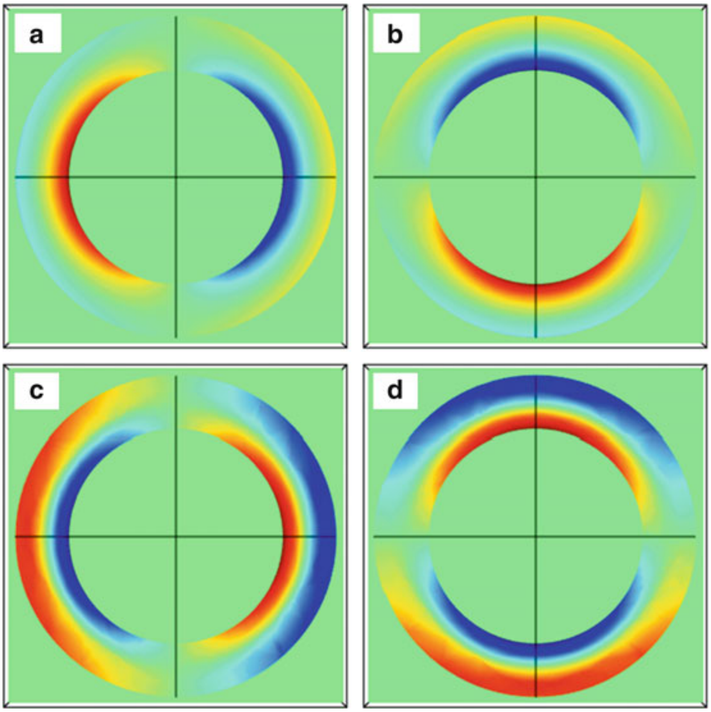

Fig. 5.5 Calculated strain components ε_{xz} (**a**) and ε_{yz} (**b**) at the first dip frequency, and ε_{xz} (**c**) and ε_{yz} (**d**) at the second dip frequency, within the $z = 0$ cross section plane within one unit cell. *Red* and *blue colors* denote positive and negative values of strain components, respectively, and *green* indicates near-zero strain

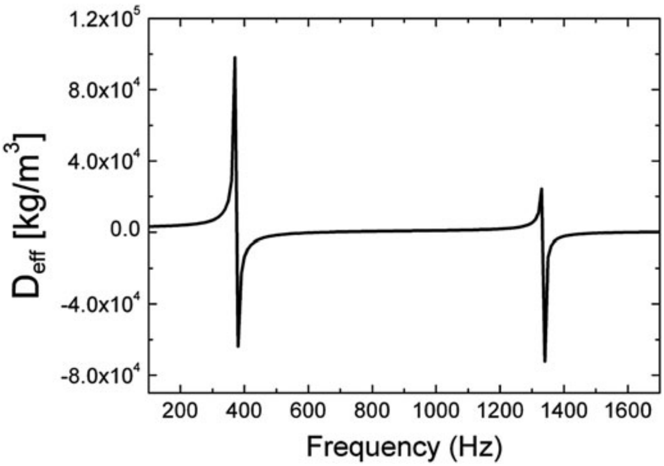

Fig. 5.6 Dynamic effective mass density D_{eff} for one unit cell of the local resonant sonic material as shown in Fig. 5.2. Around the anti-resonance frequencies (transmission dip frequencies), resonant behavior of D_{eff} is evident

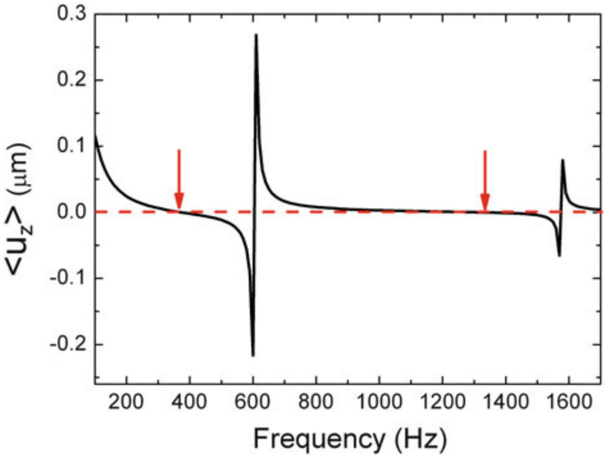

Fig. 5.7 Averaged normal surface displacement $\langle u_z \rangle$ for one unit cell of the locally resonant sonic material when a plane wave is incident along the z-direction. Large $\langle u_z \rangle$ amplitude corresponds with the transmission peak. Around the transmission dip frequency (lower side of the transmission peak frequency), $\langle u_z \rangle$ passes through zero (indicated by the *red arrows*), thereby leading to the divergence of D_{eff} as shown in Fig. 5.6

5.2.3 Physical Underpinning of the Anti-resonances

Mechanical anti-resonances constitute a very common phenomenon [14]. They are also of practical importance in mechanical systems. For example, the change in frequencies of anti-resonances can be an indicator of structural damages [15, 16]; it is also an element that needs to be taken into account in the design and modeling of the cantilever for atomic force microscopes [17–19].

By focusing on the surface normal displacement of the mechanical system, it is possible to appreciate the physical underpinning of this phenomenon. That is, an anti-resonance always occurs between two resonances. At the anti-resonance frequency, the two neighboring resonances are *simultaneously* excited but with the opposite phase, since the resonance response is given by $1/(\omega_i^2 - \omega^2)$, with ω_i denoting the angular frequency of the ith resonance and $\omega_i < \omega < \omega_{i+1}$. As the two eigenfunctions are spatially orthogonal to each other, it is possible to demonstrate that in varying the frequency continuously from ω_i to ω_{i+1}, there must be a point at which the averaged normal surface displacement is zero. In Fig. 5.7, we show the averaged normal surface displacement $\langle u_z \rangle$ at a unit cell when the incident wave is along the z-direction. It can be seen that $\langle u_z \rangle$ passes through zero at around the transmission dip frequencies, and that is the underlying mechanism of the divergence of $D_{\text{eff}} = \langle \nabla \cdot \sigma \rangle_z / (-\omega^2 \langle u_z \rangle)$ in the relevant frequency regime. It therefore follows that the dynamic mass density must have a resonant behavior at anti-resonance, giving rise to total reflection of the acoustic waves. It is also seen that

$\langle u_z \rangle$ exhibits divergent behavior at the eigenmode frequencies where the peak transmissions occur.

The understanding that the dynamic mass density's behavior–as the underlying cause of the anti-resonances–offers the possibility of generalization of this principle to the regime of ultrasound and even optical phonons. However, such experimental manifestations at high frequencies are still to be pursued.

5.3 Membrane-Type Acoustic Metamaterials

The metamaterial functionality of the locally resonant sonic materials operates only in a limited range of frequencies. Such a disadvantage can be overcome if there are membrane-type locally resonant sonic materials since one may be able to stack these membranes, each operative at a different frequency regime, so as to broaden the effective frequency range of the stacked sample.

However, making a membrane-type acoustic metamaterial that can totally reflect the low-frequency sound may seem to be anti-intuitive at first sight because a total-reflecting surface is usually a node, implying no displacement. However, a membrane is generally soft and elastically weak, hence difficult to have zero movement. But what we shall show, both theoretically and experimentally, is that precisely because of its weak elastic moduli, even a small membrane can have multiple low-frequency resonances. As there can be an anti-resonance between two resonances, it follows that the average normal displacement of the membrane vanishes at the anti-resonance frequency, thereby causing a resonant behavior of the dynamic mass density together with a diverging magnitude at the anti-resonance frequency. Total reflection occurs as a result.

It should be noted, however, that even though the average normal displacement is zero, the membrane displacement is *not* everywhere zero. But such nonzero displacement couples only to non-radiating evanescent waves, which can be ignored as far as the far-field transmission and reflection are concerned.

Below we give a detailed account of this simple system.

5.3.1 Sample Construct

In Fig. 5.8, we show our sample to consist of a circular rubber membrane decorated with a small button of varying mass (at the center of the membrane) for the purpose of tuning the eigenfrequencies [20]. These decorated membranes are assembled into a larger plate. The measurement setup, illustrated in the top panel, comprises two Brüel and Kjaer type-4206 impedance tubes with a sample sandwiched in between. The front tube has a loudspeaker at one end to generate a plane wave. There are two sensors in the front tube to sense the incident and reflected waves. The third sensor in the back tube, terminated with a 25-cm-thick anechoic sponge

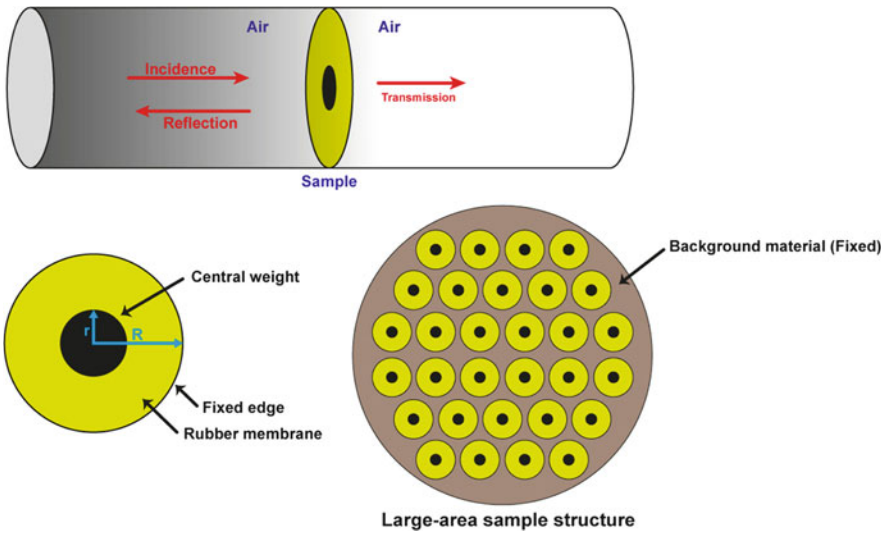

Fig. 5.8 Typical sample structure of the membrane-type acoustic metamaterial (*bottom panels*) and the testing geometry (*upper panel*)

(enough to minimize reflection), senses the transmitted wave. The signals from the three sensors are sufficient to resolve the transmitted and reflected wave amplitudes, in conjunction with their phases.

5.3.2 Vibrational Eigenfunctions and the Anti-resonance Phenomenon

In Fig. 5.9a, c, we show the finite-element COMSOL simulation results on the vibrational eigenmodes of a button-decorated rubber membrane. Here the circular button has a radius of 4.5 mm and a mass of 160 mg, and the rubber membrane is 28 mm in diameter and 0.2 mm in thickness. The mass density, Young's modulus, and Poisson's ratio for the rubber are 980 kg/m^3, 2×10^5Pa, and 0.49, respectively. A radial pre-stress, on the order of 10^5 Pa, has been applied to the membrane. The two lowest-frequency eigenmodes are shown. It is seen that for the lowest frequency eigenmode, at 250 Hz (Fig. 5.9a), the button and the membrane (on which it is attached) move in unison. However, for the mode at ~1,050 Hz (Fig. 5.9c), the button's oscillation amplitude is small whereas the surrounding rubber's oscillation amplitude is fairly significant. Figure 5.9b shows the profile at the anti-resonance frequency. It should be noted that in contrast to the 3D locally resonant sonic materials (see 5.2), in which the resonance and anti-resonance frequencies are closely grouped together, for the membrane-type acoustic metamaterials the resonance and anti-resonance frequencies are well-separated.

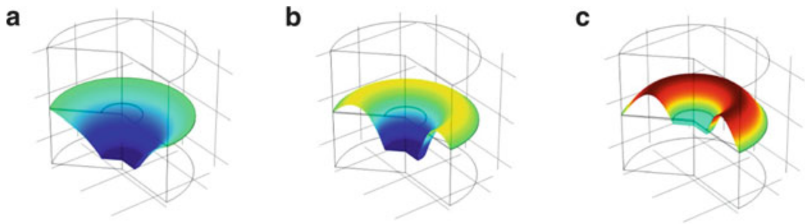

Fig. 5.9 The first eigenmode (**a**) and the second eigenmode (**c**). The profile at the dip frequency is shown in (**b**)

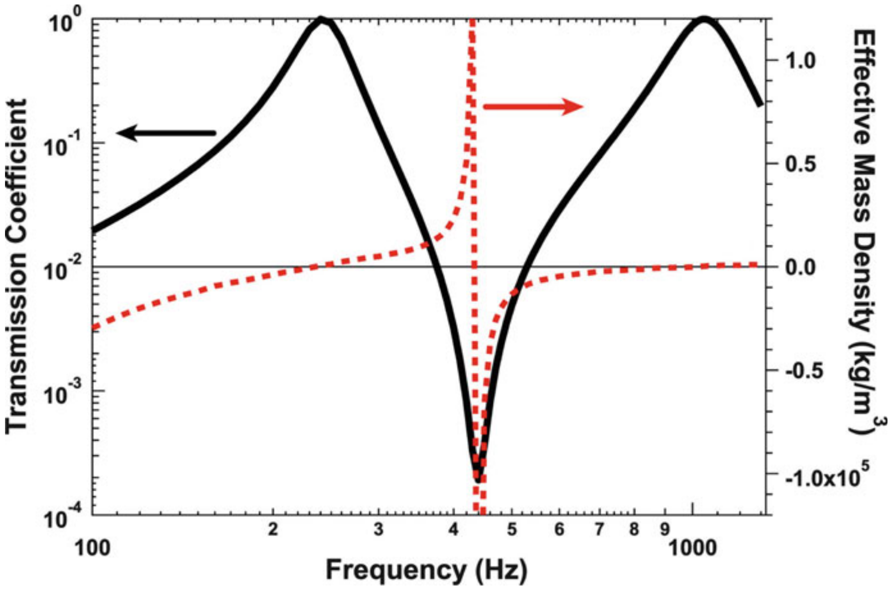

Fig. 5.10 The effective dynamic mass of the membrane-type acoustic metamaterial (*red symbols*, right axis), together with the transmission coefficient (*black solid curve*, left axis), evaluated with an incident wave with pressure modulation amplitude of 1 Pa

In Fig. 5.10, it is shown that each of the transmission peaks corresponds with an eigenmode of the system. Between the two eigenfrequencies, there is clearly a sharp dip in transmission. At this dip frequency (~440 Hz), both eigenmodes are excited, but with opposite phase. Their superposition leads to the mode profile shown in Fig. 5.9b. A closer examination of this transmission dip configuration shows that the averaged normal displacement of the mode is accurately zero. The dynamic mass density, defined as

$$D_{\mathrm{eff}} = -\langle \sigma_{zz} \rangle / (h \langle a_z \rangle) = \langle \sigma_{zz} \rangle / \left(\omega^2 h \langle w \rangle \right), \tag{5.6}$$

displays a resonance-like behavior in which D_{eff} has a divergent magnitude precisely at the anti-resonance frequency, as shown in Fig. 5.10. Here σ_{zz} denotes the zz component of the stress tensor, z being the direction normal to the membrane surface, a_z is the acceleration along the z-direction, equal to $-\omega^2 w$ for time-harmonic motions, with w being the normal displacement of the membrane and h being the thickness of the membrane. In accordance with the principle of the mass density law, if one allows the dynamic mass density to play the role of the static mass density, then total reflection should occur. However, a more accurate picture for explaining the total reflection phenomenon is as follows.

5.3.3 Anti-resonance and the Non-radiating Evanescent Mode

Consider the dispersion relation for the acoustic wave in air, $k_{||}^2 + k_{\perp}^2 = \omega^2/v^2 = (2\pi/\lambda)^2$, where $\vec{k}_{||}, k_{\perp}$ denote the wave vector components parallel or perpendicular to the surface of the membrane, respectively, $v = 340$ m/s is the speed of sound in air, and λ is the wavelength. At the air–membrane interface, we note that the normal displacement (which is usually sub-micron in magnitude and hence small compared to the membrane thickness) pattern of the membrane can be fully described by using 2D Fourier components of $\vec{k}_{||}$. If we decompose the normal displacement w into an area-averaged component and a component of whatever is left over, i.e., $w = <w> + \delta w$, then it should be clear that their respective Fourier components' magnitudes should have a distribution, illustrated schematically in Fig. 5.11. Here d denotes the lateral size of the membrane. Since d is usually much smaller than the wavelength λ, it follows that for the δw part of the displacement, the overwhelming majority of the $\vec{k}_{||}$ components will have magnitudes $|k_{||}| \geq 2\pi/d \gg 2\pi/\lambda$. Hence from the dispersion relation, it follows that the associated $k_{\perp}^2 < 0$. That is, the δw part of the displacement can only cause evanescent waves. In contrast, for the $\langle w \rangle$ part of the normal displacement, the distribution of the $|k_{||}|$ must be peaked at zero, owing to its piston-like motion. Thus again from the dispersion relation, the associated $k_{\perp}^2 \sim (2\pi/\lambda)^2$. It follows that only the average component of the normal displacement can affect far-field transmission. If $\langle w \rangle = 0$, then there can be no far-field transmission. We therefore arrive at the conclusion that total reflection is the necessary consequence of the membrane status at the anti-resonance frequency.

However, even at the anti-resonance frequency, the membrane is not stationary. Figure 5.12 displays the finite-element COMSOL simulation result at the anti-resonance frequency. It indicates evanescent waves being emitted, with a decay length on the order of a millimeter. This fact distinguishes a membrane reflector from its rigid (and heavy) wall counterpart.

In Fig. 5.10, it should be noted that before the first resonance, D_{eff} is negative with a decreasing trend (toward negative infinity) as the frequency approaches zero. This would seem to contradict the common intuition that D_{eff} should reduce to the

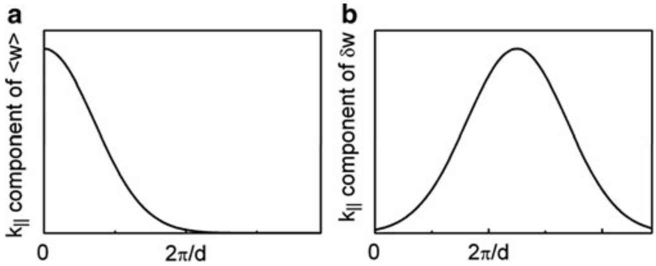

Fig. 5.11 The parallel Fourier components' distribution for (**a**) $\langle w \rangle$ and (**b**) δw components, respectively. For (**b**), the peak of the distribution lies higher than $2\pi/d$ because the feature sizes for the δw component must be smaller than d

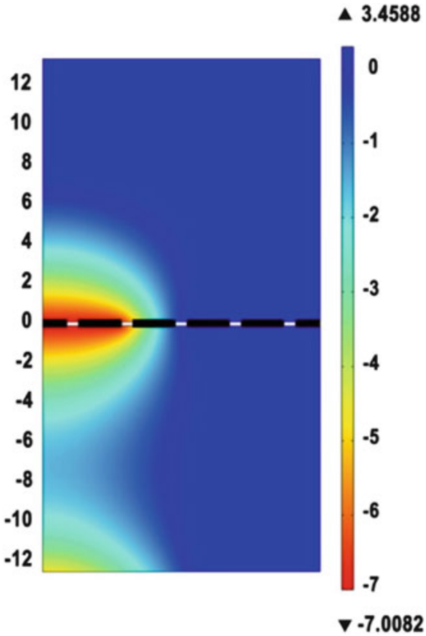

Fig. 5.12 The normal velocity field distribution near the membrane at the transmission dip frequency, where the *black dashed line* denotes the position of membrane plane. The left axis (which is also the symmetry axis) is in units of millimeter, while the velocity is in μm/s (calculated with the same incident wave intensity as that for Fig. 5.10). The wave is incident from the bottom. The decay characteristic near the two sides of the membrane surfaces indicates a decay length of 3 mm

volume-averaged value in the static limit. The fact that it does not do so in the present case is due to two factors. First, the divergent magnitude is a reflection of the boundary condition. Since the boundary of the membrane is fixed, the membrane essentially transfers its load onto the fixed boundary in the long wavelength

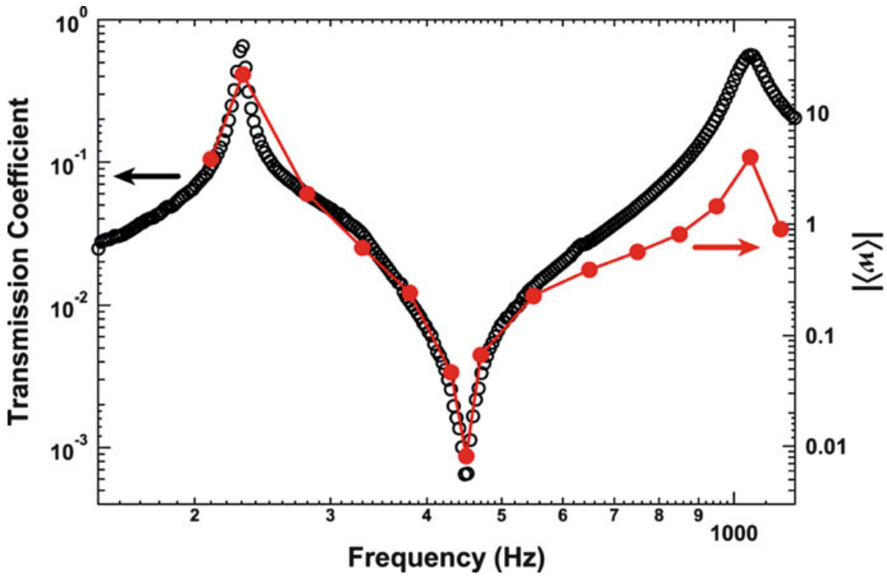

Fig. 5.13 The *black open circles* are the measured transmission coefficient (*left axis*), and the *red solid circles* are the LDV-measured $|\langle w \rangle|$(*right axis*, arbitrary unit). The *red line* is to guide the eye. A clear correlation is seen

limit. That means the fixed boundary can also be interpreted as a piece of very heavy mass. Second, the negative sign of D_{eff}, signifying off-phase response to the external force, is a reflection of Newton's third law—the reaction is opposite to the applied force. Such behavior of D_{eff}, also referred to as the "Drude-type negative mass density" in analogy to free electrons in metal, has been studied in different structures [21, 22].

5.3.4 Experimental Verification

Experimentally, we have used laser Doppler vibrometer (LDV) to directly verify the $\langle w \rangle = 0$ condition at the transmission minimum frequency. The amplitude transmission spectrum of the membrane-type metamaterial system was also measured. Both show very good agreement with the predictions of finite-element COMSOL simulations.

In Fig. 5.13 the correlation between the transmission coefficient and $|\langle w \rangle|$ is clearly demonstrated. In Fig. 5.14, we give a detailed comparison between the measured normal displacement profiles and the COMSOL simulation results on

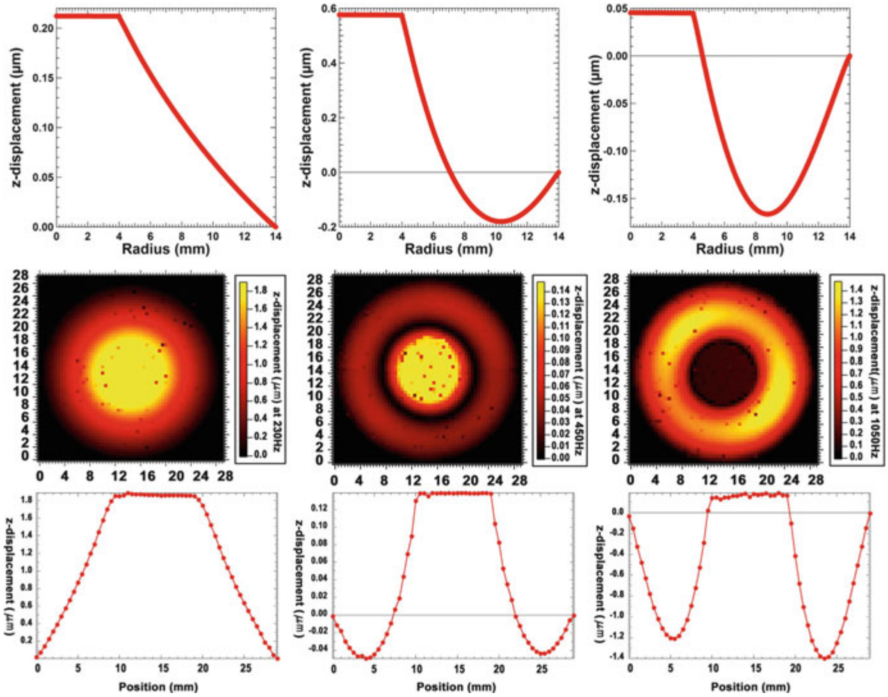

Fig. 5.14 The calculated (*upper panel*) and measured (*middle* and *lower panels*) normal displacement profiles on the two eigenmodes (left and right columns) and the anti-resonance mode (central column). The frequencies of the three profiles are (from left to right) around 230 Hz, 450 Hz, and 1,050 Hz. Displacement profiles are measured with ~0.25 Pa incident wave amplitude. Note that the simulation results (*top panels*) are only half of the experimental profiles (*bottom panels*), since the simulation results are symmetric and therefore the other half need not be shown

the two eigenmodes, together with the profile at the anti-resonance frequency. Very good agreement is seen. In particular, if one uses the experimental profile to calculate the average normal displacement, $\langle w \rangle \cong 0$ is obtained at the anti-resonance point.

In Fig. 5.15, we show a comparison of the theory and experimental transmission spectra, in which the black solid curve denotes the calculated amplitude transmission coefficient and the open circles represent measured data. The dashed red line is the prediction of the mass density law. Excellent agreement is obtained. In particular, the transmission peaks' correspondence with the vibrational eigenmodes, as well as with the transmission dip's amplitude and frequency, all conform to the theory predictions.

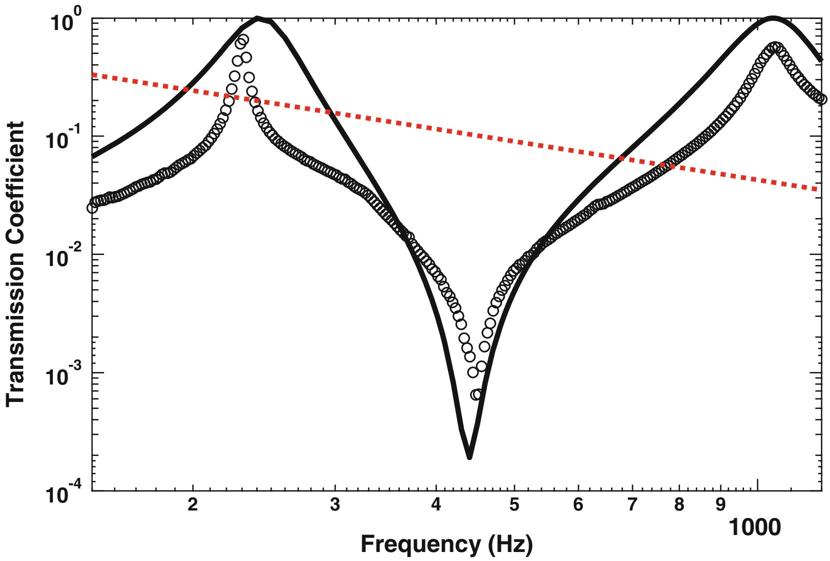

Fig. 5.15 Measured transmission coefficient amplitude (*black open circles*) and the COMSOL simulation results (*black solid curve*). The *red dashed line* is the mass density law prediction

5.3.5 Addition Rule

As stated earlier, one of the purposes of developing the membrane-type metamaterials is to stack them so as to make the stacked sample more effective at a particular frequency as well as to broaden the frequency range of the metamaterial functionality. Here we illustrate the results of such stacking to be indeed in line with what was expected.

An important point about stacking is that the membrane–membrane separation should be larger than the evanescent decay length generated by the δw part of the membrane displacement. Only when this condition is satisfied would the two membranes be regarded as truly independent, in the sense of having no near-field coupling.

We first examine quantitatively the effect of stacking two decorated membranes with the same anti-resonance frequency. In order to contrast with the traditional mass density law, we note that if the thickness of a solid wall is doubled, then the mass density law predicts the transmission amplitude to be halved, i.e.,

$$T \propto \frac{1}{\rho\omega(d+d)} = (0.5)\frac{1}{\rho\omega d}, \tag{5.7}$$

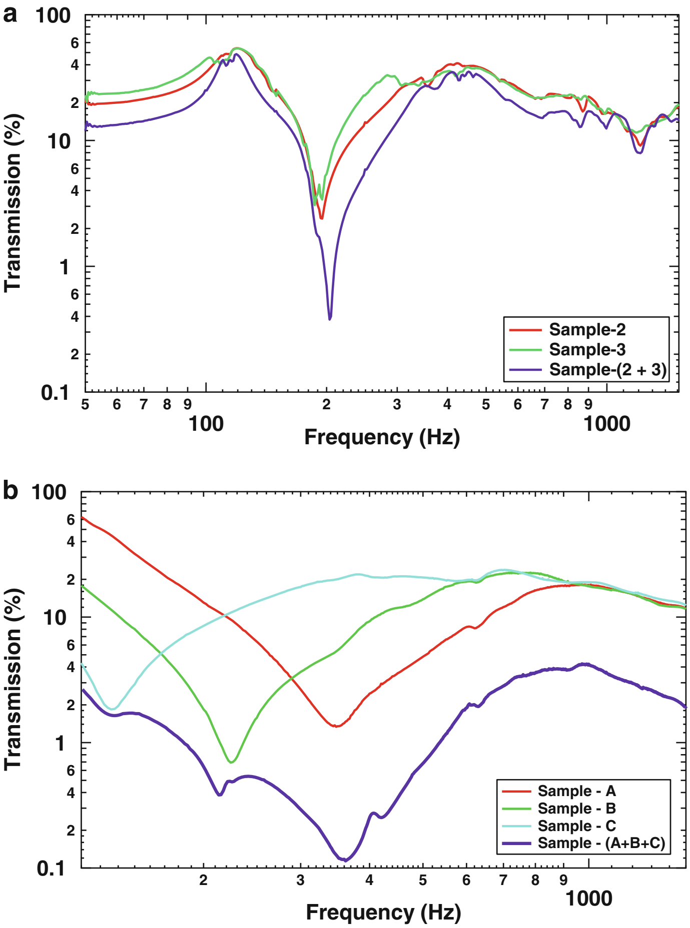

Fig. 5.16 Measured transmission spectra for stacking two membranes operating at almost identical frequencies (**a**) and three membranes operating at different anti-resonance frequencies (**b**)

a 6 dB increase in sound intensity attenuation is expected. In order to achieve 18 dB attenuation, which is the usual desired increment, it follows that the wall thickness has to be increased by a factor of 8! In contrast, for the membrane-type metamaterials, the attenuation rule is given by

$$T \propto \exp\left[-\text{const.}(d+d)\right] = \left\{\exp\left[-\text{const.}d\right]\right\}^2. \tag{5.8}$$

From the above, it can be seen that in terms of dB, the addition rule for the mass density law is logarithmic in character, whereas it is linearly additive for the membrane-type metamaterials, which is much more effective. In Fig. 5.16a,

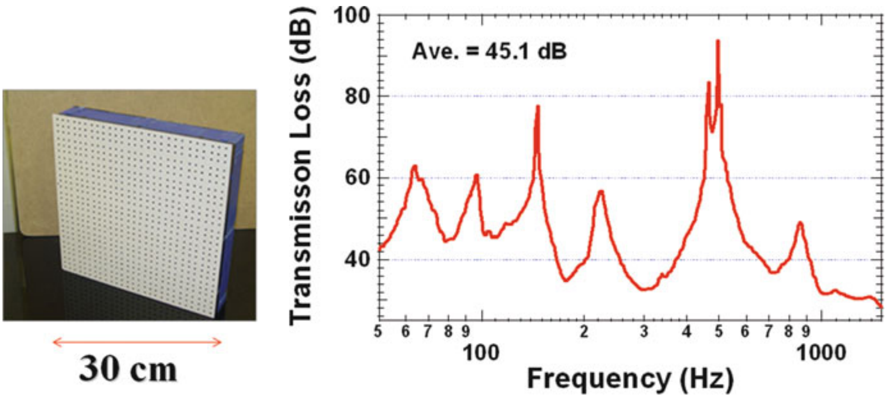

Fig. 5.17 Broadband attenuation sample (*left*) and its measured transmission loss (*right*)

we show the result of stacking two almost identical membrane-type metamaterials. The green and red curves are the transmission spectra of the two membranes, measured individually. The violet curve is the measured result by stacking the two together. At the anti-resonance frequency, almost 49 dB in intensity attenuation has been achieved. That is, stacking two nearly identical membranes shows an enhancement of ~20 dB in attenuation over a single membrane at the anti-resonance frequency.

It should be further noted that the resonant frequency of the first eigenmode is tunable by varying the weight of the central mass, in a manner that is proportional to the *inverse square root* of the central mass. The frequency of the second eigenmode, since its vibrational amplitude is mostly in the membrane, is insensitive to the weight. As the anti-resonance is a superposition of these two eigenmodes, it is viable to tune the anti-resonance frequency by varying the weight of the central mass.

To illustrate that stacking can broaden the frequency range of the membrane-type metamaterial functionality, we have fabricated a panel comprising three membranes operative at different anti-resonance frequencies. In Fig. 5.16b, the individually measured transmission spectra are shown as the red, green, and cyan curves. The transmission spectrum of the stacked sample is shown as the violet curve. The additive character of the panel is clearly seen from the remnant transmission dips of the three membranes.

To achieve broadband attenuation, we have fabricated panels with multiple weights in each unit cell (e.g., four weights in one cell). Multiple weights introduce degenerate eigenmodes, and as a result, the panel's transmission spectrum has many transmission minima. We have further tuned the frequency positions of the anti-resonance dips so that by stacking several panels, a broadband attenuation sample can be achieved. The separation between the neighboring panels is 15 mm, much larger than the evanescent decay length at the transmission dips. This sample (left panel, Fig. 5.17) has a total weight of 15 kg/m^2, and the average transmission loss is 45 dB over the 50–1,500 Hz frequency range (Fig. 5.17, right panel) [23].

5.4 Other Types of Acoustic Metamaterials

Subsequent to the initial demonstration of metamaterial characteristics of the locally resonant sonic materials, there has been a proliferation of other types of acoustic metamaterials during the past decade. This section is devoted to a brief survey of some major achievements in this field, with emphasis on the negativity in bulk modulus.

5.4.1 Negative Effective Bulk Modulus

Elastic constants play an equally important role as the mass density in determining a material's response to elastic/acoustic waves. In the context of elasticity, bulk modulus describes the elastic deformation that leads to a change in volume [24]. Intuitively, such deformation can be understood as a result of hydrostatic pressure with no preferred direction(s). This geometric characteristic of the bulk modulus, which differs from that of mass density, carries over to the consideration of effective bulk modulus (EBM) for acoustic metamaterials.

Multipole expansion is a standard technique that can be used to reveal the geometric character of the response functions. Being omnidirectional, bulk modulus-type response has the highest degree of rotational symmetry. Translated into the language of multipole representation, such response must be dominated by the monopole term [25]. On the other hand, mass density-type response is strongly directional as evidenced by the vibrational modes we analyzed in previous sections. It has the dipole symmetry.

Negativity in bulk modulus means that the medium expands under compression and contracts upon release. Thermodynamics dictates that a system with such a static response characteristic must be unstable. However, negative bulk modulus is possible in the context of dynamic response of an elastic/acoustic system, whereby the material display an out-of-phase response to an AC pressure field. Some theoretical models, such as water with suspending air bubbles [26], have been proposed for the realization of negative EBM.

In terms of experimental realization, there has been only one recipe so far that successfully achieved negative EBM [27]. The structure consists of a fluid channel that is sideway shunted by a series of periodically placed Helmholtz resonators (HRs). Instead of utilizing combinations of several materials, this metamaterial system seeks to produce modulus-type response by shaping the geometry that confines fluid in which sound propagates [28]. Several derivative works also exist on structures that display negative EBM, e.g., HRs in air that are operative in the kHz frequency regime [29, 30], and flute-like structures [31].

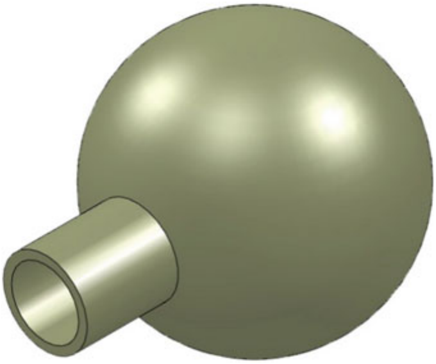

Fig. 5.18 A typical Helmholtz resonator

HR is a well-known acoustic resonance structure that can be analyzed with a spring-and-mass model. An HR is basically a bottle with a large belly and a small opening orifice, connected by a narrow neck. Since the volume of the neck is much smaller than that of the belly, it is a good approximation to consider the fluid in the neck to be incompressible. The fluid in the belly, however, is compressed when the fluid in the neck section moves inward. Once compressed, the fluid pressure in the belly naturally increases, thereby providing a restoring force. Since the wavelength of the sound is generally much larger than the dimension of the entire resonator, the pressure gradient within the cavity can be neglected. From this description of the HR, fluid in the neck serves as the mass and the belly plays the role of a spring. Using this analogy, we obtain the resonance frequency of an HR as $\omega_0^2 = k/m = (\mathrm{d}F/\mathrm{d}x)/m = S^2(\mathrm{d}P/\mathrm{d}V)/m$, with k denoting the spring constant, which can be expressed as the force (F) derivative with respect to displacement (x), and that in turn can be expressed as the pressure (P) derivative with respect to volume (V) times the square of the cross-sectional area S of the neck. By writing $m = \rho SL$, where ρ denotes fluid density and L the length of the neck, we obtain

$$\omega_0 = v\sqrt{S/VL}, \tag{5.9}$$

where $v = \sqrt{(v(dP/dv)/\rho)}$ is the speed of sound in the fluid and V is the volume of the resonator chamber (the belly) (Fig. 5.18).

The HRs in [27] were arranged orthogonal to the propagation direction of the sound in the waveguide (Fig. 5.19a). A sound wave can trigger fluid motion in the neck of an HR, and when the excitation frequency approaches the vicinity of the HR eigenfrequency, the EBM response is excited, with a typical frequency dependence of $1/(\omega_0^2 - \omega^2)$. We therefore expect a sign change in the EBM response, arising from the fact that the motion of the fluid column in the neck switches from in-phase to out-of-phase with respect to the external pressure field.

Negative bulk modulus has a similar effect on acoustic wave propagation as the negative mass density—both cause the acoustic waves to be evanescent in character.

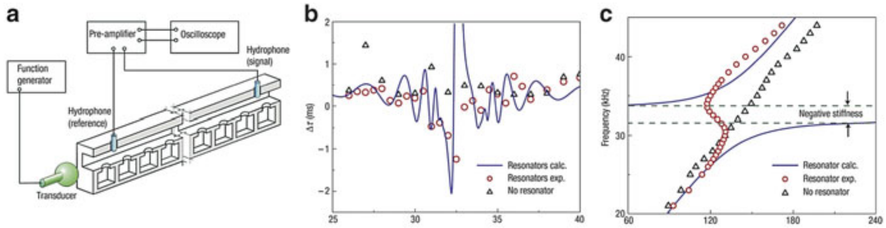

Fig. 5.19 Experimental layout (**a**) and measured results (**b**), (**c**). Negative transit time in (**b**) indicates negative group velocity, as seen in the band structure in (**c**). Figures adapted from [27]

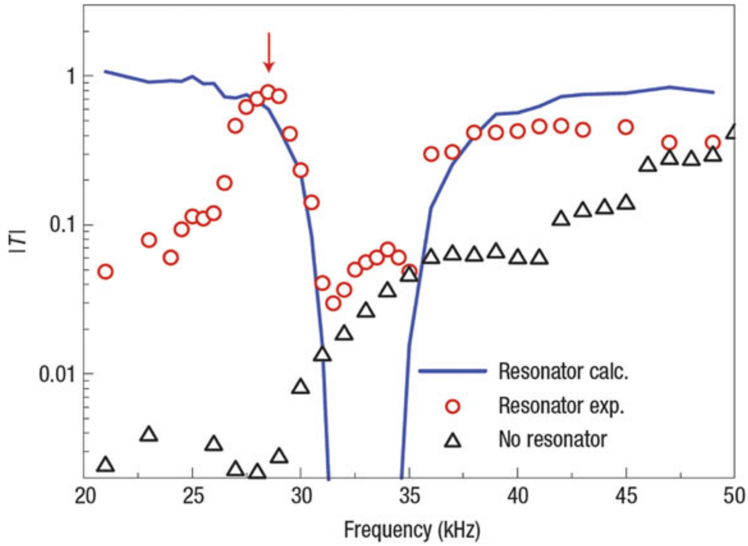

Fig. 5.20 Transmission spectra. A forbidden band is clearly seen around 32 kHz, owing to the HR resonance. The asymmetric peak (*red arrow*) is caused by Fano-like resonance, which is the consequence of interference between continuum channel and resonant channel [27, 32]. Figure adapted from [27]

Accordingly, bandgap was experimentally observed close to the resonant frequency of the metamaterial (Fig. 5.20).

5.4.2 Acoustic Double Negativity

The successful demonstrations of acoustic metamaterials with negative effective parameters naturally lead to the possibility of simultaneous double negativity in the same frequency regime. Early theoretical prediction [25] suggested that monopolar and dipolar resonances of the local scatterers are key to negative EBM and negative effective (dynamic) mass density, respectively. Recipes were conceived for their simultaneous realization [25, 26, 33, 34]. Similar to the electromagnetic case, doubly negative bulk modulus and (dynamic) mass density can lead to negative dispersion, i.e., the so-called left-handed acoustic materials. However, it was not until 2010 that the first success in experimental realization of acoustic double negativity [35] was demonstrated. In their 1D design, periodically arranged elastic membranes were deployed to tune the dipolar resonance [21], with side-opening orifices providing monopolar response [31]. Double-negative transmission band was found in the low-frequency limit. The same group later utilized the same design to demonstrate a reversed Doppler shift of sound within the double-negative band [36].

5.4.3 Focusing and Imaging

With the advent of acoustic metamaterials, a new horizon of possibilities for acoustic wave manipulation has emerged. During the past few years, there has been a proliferation of theoretical/numerical predictions [37–41] for achieving acoustic focusing and superlensing by using acoustic metamaterials. Shu Zhang et al. expanded such concept by building an interconnecting fluid network. Shunted by cavities of different volumes, each unit in the network resembles a Helmholtz resonator. It was experimentally shown that such a network is capable of achieving in-device focusing of ultrasound [42]. Lucian Zigoneanu et al. designed and fabricated flat lens with gradient index of refraction, bringing kHz airborne sound into out-of-device focus [43].

Highly dispersive materials can attain almost flat equi-frequency contours within a certain regime, thereby "canalizes" the propagation of wave [44, 45], achieving imaging effect. Such concept can be adapted to acoustic waves. By arranging locally resonant units in a square lattice, a low-frequency bandgap can emerge, with almost-flat lower band edge. It was numerically shown that the equi-frequency contour is square-like near the band edge and is capable of canalizing even evanescent acoustic wave into propagating modes [46, 47]. X. Ao and C. T. Chan took a step further [47] by incorporating rectangular lattice to introduce anisotropy. And by laying out the lattice in half-cylindrical geometry, a magnifying effect analogous to optical hyperlens [48, 49] was numerically demonstrated.

Anisotropy is at the core of the hyperlens idea. From multipole expansion, waves scattered/emanated from an object can be represented by superposition of modes with different angular momenta. Geometric details of the scatterers are carried in modes with high angular momenta that do not propagate (i.e., evanescent in character). However, for anisotropic materials in which the dielectric constant along one direction is negative, it becomes possible to have hyper-resolution. This is easy to see for a 2D circular geometry in which we have anisotropic dielectric constants $\varepsilon_\theta, \varepsilon_r$

with the condition that $\varepsilon_\theta \varepsilon_r < 0$. Then from the dispersion relation $(k_\theta^2/\varepsilon_r) + (k_r^2/\varepsilon_\theta) = (\omega^2/v^2)$, it is easy to see that both k_θ and k_r can take on very large values, implying high resolution, without violating the dispersion relation. Such a material is denoted a hyperlens [48, 50], which is able to convert evanescent waves with high angular momenta into propagating modes. An acoustic magnifying "hyperlens" was subsequently realized by Jensen Li et al. [51], based not on the negative dielectric constant but rather on the large effective density and the relatively weak bulk modulus, realized by a fan-like structure with alternating fins of brass and air ducts, so that the effective wave speed is low and thereby the relevant wavelength is small. The lens has clearly demonstrated resolution that is less than half of the wavelength (with magnification) in a spatial region that is out of the device.

In the absence of viscous effect, a longitudinal acoustic wave can propagate in ducts (i.e., waveguides) of very small cross section, without the constraint of a cutoff frequency. By exploiting this fact, and with the aid of Fabry–Perot resonances, it was shown theoretically [52] that an "acoustic endoscope" can enhance evanescent waves, therefore open the possibility for sub-diffraction imagining. This idea was subsequently realized [53] with an array of waveguides with deep-subwavelength transverse-scale size.

Besides the approaches discussed above, C. Daraio's group took a different path toward acoustic focusing—nonlinearity in granular materials [54]. They constructed a nonlinear lens by patching granular chains tightly together. Such granular chains can transform an acoustic pulse into solitary waves, whose phase velocity depends on the amplitude. By adjusting the pre-applied static force exerted on each individual chain, the lens was found able to focus sonic pulse into very high intensity.

5.4.4 Cloaking

Acoustic cloaking has attracted theoretical attention in the past few years [55–67]. In particular, researchers have conceived devices by using "transformation acoustics" as a tool. Schemes for the cloaking of acoustic surface waves [68], bending waves on thin plates [69–71] and even fluid flow [72], have been proposed theoretically and studied by numerical simulations.

The experimental breakthrough came from Fang's group [73]. By making analogy between the acoustic wave equation and the telegrapher's equation, they explored the idea of using fluid networks as a platform for realizing acoustic cloaking. The effective mass density and bulk modulus were designed to follow a gradient in the radial direction, such that the ultrasonic wave is bent around the central domain, thereby minimizing the scattering of the object placed inside the domain so as to render it "invisible" to external observers. Experimental demonstration has clearly shown the reduced shadowing effect of the scattering object in the presence of the cloak. Impedance mismatch and the inevitable dissipative loss accounted for the less-than-perfect cloaking effect. Recently, the method of transformation acoustics showed its power in the design and experimental realization of an acoustics “carpet cloak” in air [74].

5.4.5 Acoustic Rectification

Time-reversal symmetry and spatial inversion symmetry are intrinsic to linear acoustic wave equation. Hence, nonreciprocal transmission of wave requires certain extra conditions to break these symmetries. By introducing second harmonics (nonlinear effect) into the wave equation and thereby breaking its time-reversal symmetry, an acoustic one-way mirror was proposed [75]. This was subsequently realized in the ultrasonic regime [76]. More recently, C. Daraio’s group used 1D, strongly nonlinear (force-loaded) artificial granular medium to achieve rectification of acoustic waves and proposed prototypes of mechanical logic gates [77]. On the other hand, acoustic “one-way mirror” was also realized using simple 2D phononic crystals with incomplete bandgap [78]. Li et al. incorporated diffraction structures on one end of the phononic crystal to induce spatial modes with different *k*-vectors, thereby mimicking the condition of oblique incidence to result in transmission for part of the acoustic energy.

5.4.6 Hybrid Elastic Solids

Negativity in the effective mass density and the EBM is a direct outcome of dipolar and monopolar resonances, respectively. A natural question is whether it is possible to have a solid with a unit cell that can display monopole, dipole, and quadrupole resonances [6]. If so, what kind of behavior would such a solid exhibit? A recent publication [79] has proposed a unit cell design that can realize all three resonances, with overlapping resonance frequency regimes. Finite-element calculations found this unique design to simultaneously support dipolar and monopolar/quadrupolar resonances. As a result, two doubly negative bands exist. In one band, with overlapping dipolar and monopolar resonances, only pressure waves can propagate (with negative dispersion) while the shear waves are evanescent. This in effect resembles the acoustic property of a fluid. In the other band, “super-anisotropic behavior” is exhibited—i.e., pressure and shear waves are allowed to propagate only along mutually perpendicular directions. Hence within the frequency range of this band, the material appears to be a rigid solid in one direction but appears fluid-like in the other (Table 5.1).

Table 5.1 Properties of the hybrid elastic solids [79]

Direction	ΓX		ΓM	
Wave type	P-wave	S-wave	P-wave	S-wave
Wave velocities	$\sqrt{\frac{\kappa_{\text{eff}}+\mu_{\text{eff}}}{\rho_{\text{eff}}}}$	$\sqrt{\frac{c_{44}^{\text{eff}}}{\rho_{\text{eff}}}}$	$\sqrt{\frac{\kappa_{\text{eff}}+c_{44}^{\text{eff}}}{\rho_{\text{eff}}}}$	$\sqrt{\frac{\mu_{\text{eff}}}{\rho_{\text{eff}}}}$
Lower band $\kappa_{\text{eff}}>0, \rho_{\text{eff}}<0$ $\mu_{\text{eff}} \ll 0, c_{44}^{\text{eff}}>0$	Propagation allowed, double negative in ρ_{eff} and μ_{eff}	Evanescent, negative ρ_{eff}	Evanescent, negative ρ_{eff}	Propagation allowed, double negative in ρ_{eff} and μ_{eff}
Higher band $\kappa_{\text{eff}}<0, \rho_{\text{eff}}<0$ $\mu_{\text{eff}}>0, c_{44}^{\text{eff}}>0$	Propagation allowed, double negative in ρ_{eff} and κ_{eff}	Evanescent, negative ρ_{eff}	Propagation allowed, double negative in ρ_{eff} and κ_{eff}	Evanescent, negative ρ_{eff}

5.5 Dynamic Mass Density at the Low-Frequency Limit

It is well known that for a time-harmonic wave, the elastic wave equation may be written as

$$\nabla \cdot \mu[\nabla\vec{u} + (\nabla\vec{u})^{\text{T}}] + \nabla(\lambda\nabla \cdot \vec{u}) + D\omega^2\vec{u} = 0, \tag{5.10}$$

where D is the mass density, λ and μ are the (spatially varying) Lamé constants, $\vec{u}$ is the displacement vector, and $(\nabla\vec{u})^{\text{T}}$ denotes the transpose of the tensorial quantity $\nabla\vec{u}$. Static effective elastic moduli and mass density are usually defined in the zero-frequency limit, where the limit $\omega \to 0$ is usually taken *first*, so that the mass density term drops out. Thus, the *static* effective moduli are obtained by the homogenization of $\nabla \cdot (\mu\nabla)$ and $\nabla(\lambda\nabla\cdot)$ operators. In contrast, to obtain the dynamic mass density expression, we have to solve the wave equation (5.10) so as to get the low-frequency wave solution and its relevant dispersion relation $\omega(\vec{k})$. The fact that for the fluid–solid composites the two limits are not necessarily the same has already been explained in the introductory Sect. 5.1. Thus the dynamic mass density is obtained from the slope of $\omega(\vec{k})$, i.e., the wave velocity. However, to separate out the elastic constant and mass density information from a single wave speed requires an additional criterion, which turns out to be the different angular momentum channels, as shown below. But at this point, we must first briefly introduce the MST, since our approach in obtaining the $\omega \to 0$ dynamic mass density is simply to examine the low-frequency limit of the MST.

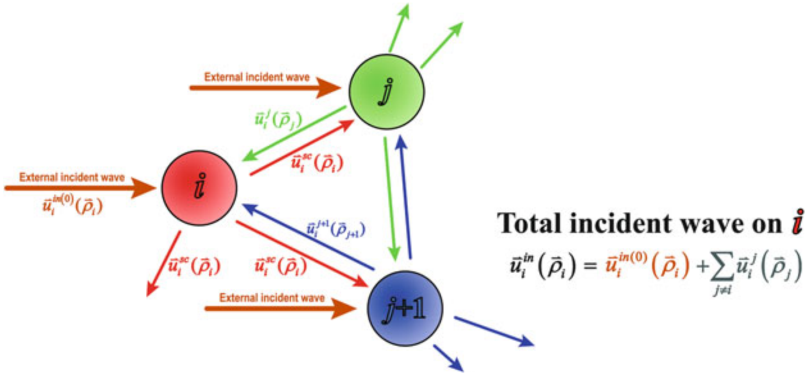

Fig. 5.21 A schematic diagram illustrating the basic idea of the multiple-scattering theory (MST), in which the scattered outgoing wave from any one particular scatterer constitutes part of the incident wave to any other scatterer

5.5.1 Multiple-Scattering Theory

MST represents a solution of the elastic wave equation (5.10) for a periodic composite that accounts fully for *all* the multiple scattering effects between *any* two scatterers, shown schematically in Fig. 5.21, as well as for the inherent vector character of elastic waves [2, 80, 81]. In what follows, we shall attempt to illustrate the basic ideas of the MST by using diagrammatic illustrations. A more detailed mathematical description can be found in Chap. 10.

We shall focus on the case of 2D periodic composites with a fluid matrix, in which MST has a rather simple form, as shown in Fig. 5.22, where $\vec{u}_i^{\text{in}}(\vec{\rho}_i) = \sum_n a_n^i \vec{J}_n^i(\vec{\rho}_i)$ and $\vec{u}_i^{\text{sc}}(\vec{\rho}_i) = \sum_n b_n^i \vec{H}_n^i(\vec{\rho}_i)$ are the waves incident on, and scattered by the scatterer i, respectively, with $\alpha_1 = \omega\sqrt{D_1/B_1}$ being the wave vector in the fluid matrix. Here D_1 and B_1 denote the mass density and bulk modulus of the matrix, respectively, $\vec{\rho} = (\rho, \varphi)$ is the polar coordinates, and $J_n(x)$ and $H_n(x)$ denote the nth Bessel function and Hankel function of the first kind, respectively.

Since the incident wave on scatterer i comprises the external incident wave $\vec{u}_i^{\text{in}(0)}(\vec{\rho}_i)$ plus the scattered waves by all the other scatterers except i (as shown in Fig. 5.21), we have

$$\vec{u}_i^{\text{in}}(\vec{\rho}_i) = \vec{u}_i^{\text{in}(0)}(\vec{\rho}_i) + \sum_{j\neq i} \sum_{n''} b_{n''}^j \vec{H}_{n''}^j(\vec{\rho}_j), \tag{5.11}$$

where $\vec{\rho}_i$ and $\vec{\rho}_j$ refer to the position of the same spatial point measured from scatterers i and j, respectively.

In Fig. 5.22, the expansion coefficients $\{a_n\}$ and $\{b_n\}$ are not independent but are in fact related by the so-called T matrix. This is shown in Fig. 5.23, where $T = \{T_{nn'}\}$ is the elastic Mie scattering matrix determined by matching the normal displacement and normal stress component at the fluid–solid interface.

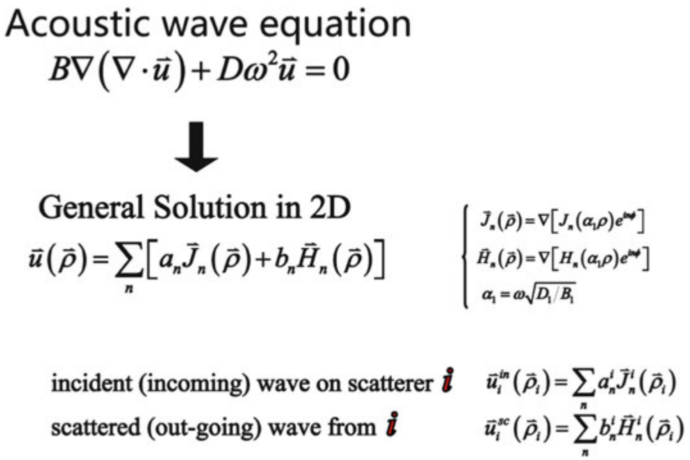

Fig. 5.22 General solution of the acoustic wave equation for 2D phononic crystals with a fluid matrix. Here J_n denotes the Bessel function of nth order and H_n denotes the nth-order Hankel function of the first kind

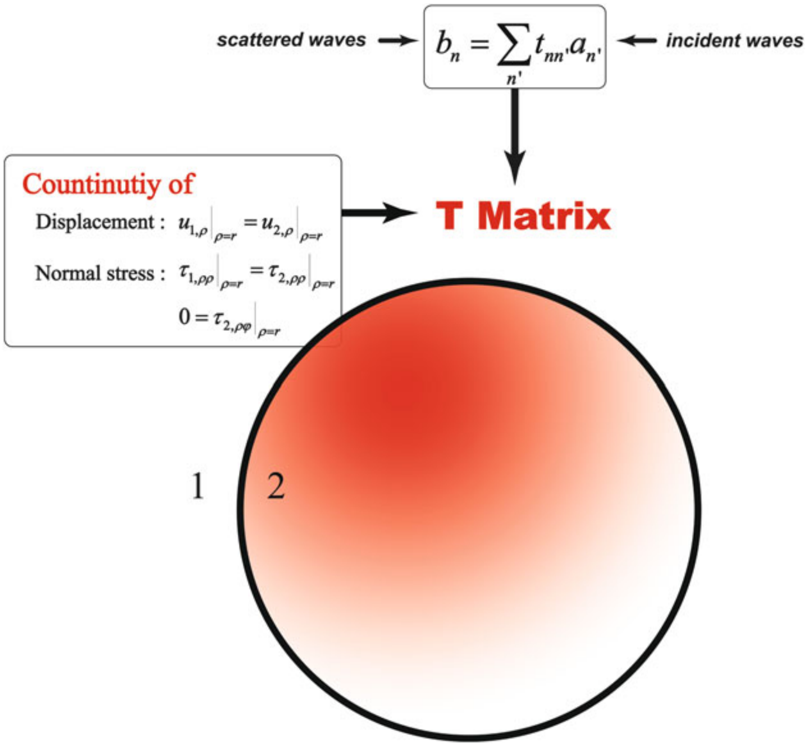

Fig. 5.23 T matrix and the boundary conditions. Region 1 denotes the matrix materials and region 2 denotes the solid scatterer

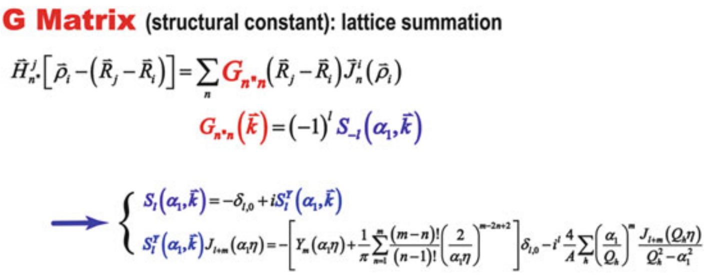

Fig. 5.24 G matrix and its evaluation method

With the help of addition theorem, it can be proved that

$$\vec{H}^j_{n''}(\vec{\rho}_j)=\vec{H}^j_{n''}\left(\vec{\rho}_i-(\vec{R}_j-\vec{R}_i)\right)=\sum_n G^{ij}_{n''n}\vec{J}^i{}_n(\vec{\rho}_i), \tag{5.12}$$

where the G matrix $G^{ij}_{n''n}=G_{n''n}(\vec{R}_j-\vec{R}_i)$ denotes the translation coefficients as shown in Fig. 5.24, with $\phi=\arg(\vec{R}_j-\vec{R}_i)$, $\vec{R}_{i(j)}$ being the position of scatterer $i(j)$. This translation means that the wave scattered by the scatterer j may be expressed in terms of Bessel functions centered at scatterer i. And since the coefficients $\{a_n\}$ and $\{b_n\}$ at scatterer i are related by the T matrix, one can therefore obtain a single matrix equation with $\{a_n\}$ being the variables. Of course, in such a derivation, it is assumed that in a periodic composite every scatterer is the same.

For the purpose of calculating the dispersion relation, we do not need an externally incident wave $\vec{u}_i^{\mathrm{in}(0)}(\vec{\rho}_i)$ in (5.2), thus we have

$$\vec{u}_i^{\mathrm{in}}(\vec{\rho}_i)=\sum_{j\neq i}\sum_{n''}b^j_{n''}\vec{H}^j_{n''}(\vec{\rho}_j). \tag{5.13}$$

After substituting the expressions for the T matrix and G matrix into this equation and Fourier-transforming the coefficients of $\{a_n\}$, as shown in Fig. 5.25, we arrive at the following secular equation:

$$\det\left|T^{-1}_{nn'}-G_{nn'}(\vec{k})\right|=0. \tag{5.14}$$

Equation (5.14) is equivalent to (85) in Chap. 10. Written in this particular form, (5.14) is particularly suitable for the low-frequency expansion, as seen below.

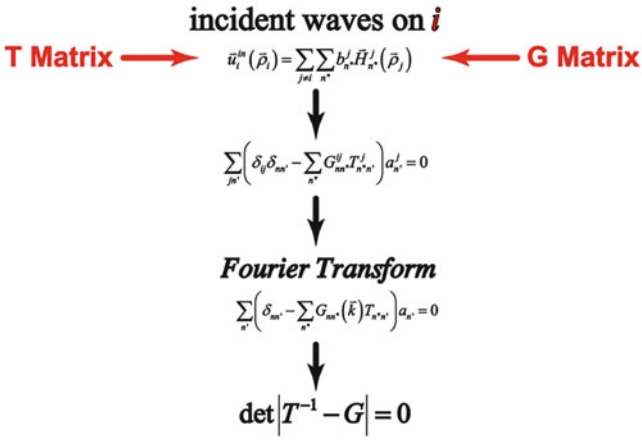

Fig. 5.25 Secular determinant equation of the MST, for the determination of band structures for periodic composites

5.5.2 *Dynamic Mass Density at the* ω → *0 Limit*

Equation (5.14) is the secular equation for determining the band structure of a periodic composite. Here we want only the branch at the $\omega \to 0$ limit, i.e., by letting $\alpha_1 \to 0$ and retaining the leading-order terms of the secular equation. This is illustrated in Fig. 5.26.

By taking the low-frequency limit and retaining terms to the order of ω^{-2}, both the T^{-1} matrix and the G matrix can be simplified to 3×3 matrices [4, 5]. Therefore, the secular equation in the low-frequency limit is given by

$$\det \begin{vmatrix} \dfrac{D_1+D_2}{D_1-D_2}+\dfrac{x^2 f}{1-x^2} & \dfrac{ixf}{1-x^2} & -\dfrac{f}{1-x^2} \\ -\dfrac{ixf}{1-x^2} & \dfrac{B_2}{B_2-B_1}+\dfrac{x^2 f}{1-x^2} & \dfrac{ixf}{1-x^2} \\ -\dfrac{f}{1-x^2} & -\dfrac{ixf}{1-x^2} & \dfrac{D_1+D_2}{D_1-D_2}+\dfrac{x^2 f}{1-x^2} \end{vmatrix} = 0, \quad (5.15)$$

in which $f = \pi r_0^2/A$ is the filling ratio of the solid inclusions, $B_1 = \lambda_1$ and $B_2 = \lambda_2 + \mu_2$ are the bulk moduli of the fluid matrix and solid inclusions, respectively, and $x = V_{\text{eff}}/V_1$ is the variable to be solved in the determinant equation (5.15). By discarding the trivial root, we obtain the effective sound velocity of the composite as

Low-frequency limit, $\alpha_1 \to 0$

$$J_0(\alpha_1 r_0) \to 1 - \frac{1}{4}\alpha_1^2 r_0^2 \qquad H_0(\alpha_1 r_0) \to 1 - \frac{1}{4}\alpha_1^2 r_0^2 + i\frac{2}{\pi}\ln(\alpha_1 r_0) + i\frac{2}{\pi}(\gamma_0 - \ln 2)$$

$$J_1(\alpha_1 r_0) \to \frac{1}{2}\alpha_1 r_0 - \frac{1}{16}\alpha_1^3 r_0^3 \qquad H_1(\alpha_1 r_0) \to \frac{1}{2}\alpha_1 r_0 - \frac{1}{16}\alpha_1^3 r_0^3 - i\frac{2}{\pi}\frac{1}{\alpha_1 r_0} + i\frac{\gamma_0 - \frac{1}{2}}{\pi}\alpha_1 r_0$$

$$J_2(\alpha_1 r_0) \to \frac{1}{8}\alpha_1^2 r_0^2 - \frac{1}{96}\alpha_1^4 r_0^4 \qquad H_2(\alpha_1 r_0) \to \frac{1}{8}\alpha_1^2 r_0^2 - \frac{1}{96}\alpha_1^4 r_0^4 - i\frac{4}{\pi}\frac{1}{\alpha_1^2 r_0^2} - i\frac{1}{\pi}$$

$$\ldots\ldots \qquad \ldots\ldots$$

$$\longrightarrow \quad T^{-1} = -I + \frac{4i}{\pi r_0^2}\frac{1}{\alpha_1^2}\begin{bmatrix} \frac{D_1+D_2}{D_1-D_2} & 0 & 0 \\ 0 & \frac{\lambda_2+\mu_2}{\lambda_2+\mu_2-\lambda_1} & 0 \\ 0 & 0 & \frac{D_1+D_2}{D_1-D_2} \end{bmatrix}$$

$$G = -I + \frac{4i}{A}\frac{1}{1-x^2}\frac{1}{\alpha_1^2}\begin{bmatrix} -x^2 & xe^{-i\theta_0} & e^{-2i\theta_0} \\ -xe^{i\theta_0} & -x^2 & -xe^{i\theta_0} \\ e^{2i\theta_0} & -xe^{i\theta_0} & -x^2 \end{bmatrix}$$

Fig. 5.26 The T^{-1} matrix and G matrix in the low-frequency limit, where r_0 and A are the radius of solid inclusions and area of unit cell, respectively. λ_1, λ_2, and μ_2 are the Lamé constants, and $\gamma_0 \approx 0.5772$ is the Euler's constant. θ_0 Is the polar angle of wave vector $\vec{k}$, which vanishes in the determinant evaluation of $\left|T^{-1} - G\right|$. The variable $x = V_{\text{eff}}/V_1$ is the quantity to be evaluated

$$V_{\text{eff}} = \sqrt{\frac{B_{\text{eff}}}{D_{\text{eff}}}} = \sqrt{\frac{\frac{B_2}{B_2 + (B_1 - B_2)f}B_1}{\frac{(D_2 + D_1) + (D_2 - D_1)f}{(D_2 + D_1) - (D_2 - D_1)f}D_1}}. \tag{5.16}$$

It is well known that according to the effective medium theory [82], the EBM B_{eff} of the fluid–solid composite is given by

$$\frac{1}{B_{\text{eff}}} = \frac{1-f}{B_1} + \frac{f}{B_2} \tag{5.17}$$

or

$$B_{\text{eff}} = \frac{B_2}{B_2 + (B_1 - B_2)f}B_1. \tag{5.18}$$

It can also be seen from Eq. (5.15) and Fig. 5.26 that the expression for B_{eff}, (5.18), arises from the $n = 0$ angular scattering channel.

By using (5.16) and the effective medium expression for B_{eff} [i.e., (5.18)], we arrive at precisely the Berryman effective mass density in 2D [83, 84]:

$$D_{\mathrm{eff}} = \frac{(D_2 + D_1) + (D_2 - D_1)f}{(D_2 + D_1) - (D_2 - D_1)f} D_1. \tag{5.19}$$

In contrast to the B_{eff} expression, the effective mass density D_{eff} is completely determined by the $n = 1$ angular channel. As pointed out previously, the effective mass density and the EBM represent *separate* but parallel wave scattering channels.

Equation (5.19) is valid for both the square and the hexagonal lattices when the filling fraction of the solid inclusions is not very high. At this leading order of density expansion, both B_{eff} and D_{eff} are noted to be independent of the lattice structure. In particular, they are both relatively accurate for *random* fluid–solid composites as long as the density is not close to the tight-packing limit, and the viscous boundary layer thickness is smaller than the fluid channel width. When the concentration of scatterers becomes larger and larger, it is expected that higher-order angular momentum channels in T^{-1} and G matrices should be included. The effective sound speeds would then be different for the square and the hexagonal lattices, but isotropy still holds.

It is instructive to carry the effective dynamic mass density evaluation to a higher concentration level, by retaining more angular momentum channels in the T^{-1} and G matrices. Through a lengthy derivation, the dynamic mass density is found to be in the form [84–86]

$$D_{\mathrm{eff}} = \frac{(D_2 + D_1) + (D_2 - D_1)(f - g)}{(D_2 + D_1) - (D_2 - D_1)(f + g)} D_1, \tag{5.20}$$

where [87]

$$g = 768 \left(\frac{M_4}{\pi} \right)^2 f^4 \approx 0.3058 f^4 \tag{5.21}$$

for the square lattice, and

$$g = 1{,}620 \left(\frac{M_6}{\pi^2} \right)^2 f^6 \approx 0.0754 f^6 \tag{5.22}$$

for the hexagonal lattice. Here the lattice sums

$$M_4 = \sum_{h \neq 0} \frac{J_4(K_h a)}{(K_h a)^2} \mathrm{e}^{4\mathrm{i}\theta_h} \tag{5.23}$$

and

$$M_6 = \sum_{h \neq 0} \frac{J_6(K_h a)}{(K_h a)} \mathrm{e}^{6\mathrm{i}\theta_h} \tag{5.24}$$

are defined in the reciprocal spaces of the square and hexagonal lattices, respectively, with $\vec{K}_h = (K_h, \theta_h)$ denoting the reciprocal lattice vector in polar coordinates and a being the lattice constant. In contrast, the EBM is still given by (5.18), i.e., the Wood's formula.

Comparing (5.20) with (5.19), we notice that the effective mass density is modified by a correction term, g. When the filling fraction of the inclusions is not very high, g is very small so that it can be safely neglected. When this happens, (5.20) reduces to (5.19), i.e., the dipole solution. However, in case of high concentration of inclusions, Berryman's expression, i.e., (5.19), should be modified to incorporate the influence of higher-order scattering coefficients.

It is worth noting that the correction term g is proportional to f^4 for the square lattice and to f^6 for the hexagonal lattice. Common sense tells us that the correction term should be quadratic in f, but here the correction term g is obviously determined by the symmetry of the square and hexagonal lattices. This point can be easily understood since the coefficients in front of f^4 (square lattice) and f^6 (hexagonal lattice) are respectively the lattice sums M_4 and M_6 defined by (5.23) and (5.24), and they are clearly determined by the lattice symmetry.

If the matrix is made of solid instead of liquid, we can also take the low-frequency limit on the MST in a similar way. But a different effective medium formula for the mass density may be expected since in a solid matrix not only the longitudinal wave but also the transverse waves can propagate. It is well known that in 2D phononic crystals, when the wave vector is confined in the 2D plane (i.e., the x–y plane) perpendicular to the cylinder axis direction (i.e., the z-direction), the elastic waves can be decoupled into an out-of-plane transverse z mode and an in-plane mixed xy mode.

For the transverse z mode, the displacement is perpendicular to the x–y plane and thus easier to deal with. By taking the low-frequency limit and retaining the dominant terms, the $T^{-1} - G$ matrix can also be simplified to a 3×3 matrix [5]:

$$T^{-1} - G = \frac{4i}{\pi r^2} \frac{1}{\beta_1^2} \begin{bmatrix} \dfrac{\mu_2 + \mu_1}{\mu_2 - \mu_1} + f \dfrac{x^2}{1 - x^2} & \dfrac{ixf}{1 - x^2} \mathrm{e}^{-\mathrm{i}\theta_0} & -\dfrac{f}{1 - x^2} \mathrm{e}^{-2\mathrm{i}\theta_0} \\ -\dfrac{ixf}{1 - x^2} \mathrm{e}^{\mathrm{i}\theta_0} & \dfrac{D_1}{D_1 - D_2} + f \dfrac{x^2}{1 - x^2} & \dfrac{ixf}{1 - x^2} \mathrm{e}^{-\mathrm{i}\theta_0} \\ -\dfrac{f}{1 - x^2} \mathrm{e}^{2\mathrm{i}\theta_0} & -\dfrac{ixf}{1 - x^2} \mathrm{e}^{\mathrm{i}\theta_0} & \dfrac{\mu_2 + \mu_1}{\mu_2 - \mu_1} + f \dfrac{x^2}{1 - x^2} \end{bmatrix}, \tag{5.25}$$

in which $x = V_{\text{eff}}/V_1$ is the quantity to be evaluated. By solving (5.25), we obtain the effective transverse wave velocity of the composite as

$$V_{\text{eff}} = \sqrt{\frac{\mu_{\text{eff}}}{D_{\text{eff}}}} = \sqrt{\frac{\frac{(\mu_2 + \mu_1) + (\mu_2 - \mu_1)f}{(\mu_2 + \mu_1) - (\mu_2 - \mu_1)f}\mu_1}{(1-f)D_1 + fD_2}}. \tag{5.26}$$

It can be recognized from (5.26) that the effective shear modulus μ_{eff}, determined by the $n = 1$ angular channel [see (5.25)], is given by

$$\mu_{\text{eff}} = \frac{(\mu_2 + \mu_1) + (\mu_2 - \mu_1)f}{(\mu_2 + \mu_1) - (\mu_2 - \mu_1)f}\mu_1. \tag{5.27}$$

It is interesting to point out that (5.27) has the same form as (5.19), and this similarity is due to the fact that both μ_{eff} and D_{eff} arise from the $n = 1$ angular channel scattering.

According to (5.26) and the effective shear modulus expression for μ_{eff}, i.e., (5.27), we arrive at the volume-averaged mass density expression for the transverse z mode:

$$D_{\text{eff}} = \rho_{\text{eff}} = (1-f)D_1 + fD_2, \tag{5.28}$$

which is distinct from the fluid-matrix case. Here the effective mass density for the solid-matrix composite is determined by the $n = 0$ angular channel. Equation (5.28) for the solid matrix case is noted to be identical to that found by Berryman [83] through a different approach.

If we let $\mu_1 \to 0$, then according to (5.27), we have $\mu_{\text{eff}} \to 0$. That is, when the solid matrix is gradually reduced to the limit of zero shear modulus, the whole composite would also act like a zero-shear modulus system, i.e., the composite behaves like a fluid. However, it is important to note that even in this limit, the volume-averaged density formula, i.e., (5.28), still holds. Therefore, by first taking the $\omega \to 0$ limit and then the $\mu_1 \to 0$ limit, we arrive at the volume-averaged mass density expression. However, reversing the order of taking the two limits leads to the expression given by (5.19). Therefore, the order of taking the two limits *cannot* be interchanged, as explained in the introductory Sect. 5.1.

5.5.3 Comparison with Experimental Data

Cervera et al. have measured the sound velocity in a 2D phononic crystal composed of hexagonal array of aluminum cylinders in air [86]. Here the frequency of sound is 600 Hz, and the wavelength of sound in air, 57 cm, is much larger than either the cylinder diameter or the lattice constant. The wavelengths of sound in Al, for both longitudinal and transverse waves, are even larger. The use of effective medium theory is thus justified. The viscosity and mass density of air at normal temperature are 1.827×10^{-5}Pa s and 1.292 kg/m^3, respectively. At the experimental frequency of ~600 Hz, the viscous boundary layer thickness $\ell_{\text{vis}} = \sqrt{\eta/\rho_{\text{air}}\omega} = 6.12 \times 10^{-3}$ cm is much smaller than either the cylinder diameter, the lattice constant, or the fluid channel width ℓ. Thus the condition $\ell \gg \ell_{\text{vis}}$ is valid.

In the experiment, the maximum filling ratio of Al cylinders is about 0.36, shown as open triangles in Fig. 5.27, where it can be seen that there is nearly an order of magnitude discrepancy between the experimentally measured velocity with that predicted by using the volume-averaged mass density and the EBM B_{eff} given by (5.18). In contrast, when the dynamic effective mass density, (5.19), is used, excellent agreement is seen.

For higher filling ratio of Al cylinders, we have used COMSOL Multiphysics, a finite-element solver, to perform a band-structure calculation for the same periodic system. From the band structure, i.e., the dispersion relation, one can compute the effective wave speed by using $c = \omega/k$ in the low-frequency limit. The corresponding results are plotted in Fig. 5.27 in green circles. They are seen to be in excellent agreement with (5.20), as shown with red solid curve, where the correction term g is included.

In Fig. 5.28a, we show the numerically calculated displacement field intensities for the relevant experiment. It can be seen that the displacement field is nearly zero inside the cylinders, hence it is almost impossible to have the condition for the validity of volume-averaged density formula. However, when the impedance mismatch is relatively moderate, e.g., when the mass density contrast is small, then the effective dynamic mass density reduces the volume-averaged mass density, which means that the static mass density is a special case of the dynamic mass density. For comparison with Fig. 5.28a, we have also plotted the displacement field intensities for the poly(methyl methacrylate) (PMMA)–water system in Fig. 5.28b, in which the wavefield homogeneity is very evident. As our derivation of the dynamic mass density is obtained by taking the long wavelength limit of the scattering wave field solutions, it is not surprising that such formula inherently accounts for the wavefield inhomogeneities as they exist in reality. As explained in Sect. 5.1, the *relative motion* between the components of a composite is the basic reason leading to the difference between the static and dynamic mass densities, and such relative motion is evident when the impedance mismatch is large and $\ell >> \ell_{vis}$.

In a solid-matrix composite, the presence of a nonzero shear modulus for the matrix component means that in the long wavelength limit, uniform motion of the matrix and the inclusions is guaranteed. As a result, the dynamic mass density for the solid-matrix composites is always the volume-averaged value. When one further takes the limit of $\mu_1 \to 0$ in that case, only the relative ratio of the longitudinal wavelength to the transverse (shear) wavelength is altered, which is the reason that the effective mass density expression still remains the same as the static mass density.

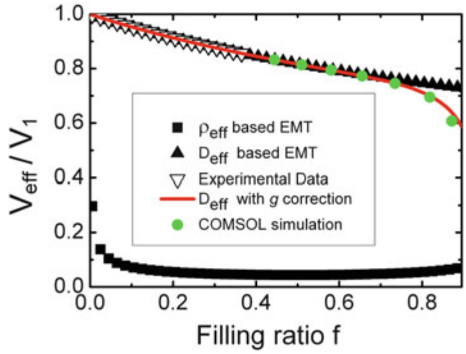

Fig. 5.27 The effective sound velocities calculated with the effective bulk modulus given by Wood's formula with volume-averaged mass density (*solid squares*) and with the mass density given by (5.19) (*solid triangle*). Experimentally measured effective sound velocity is shown as open triangles. While the volume-averaged mass density gives results very far removed from the experiment, the mass density given by (5.19) is shown to yield almost perfect agreement with measured results when the filling ratio of the Al cylinders is not very high. When the filling ratio is larger than 0.6, however, the correction term g should be included [see (5.20)], with the prediction shown by the *red solid curve*. It can be seen that the prediction of (5.20) agrees very well with the finite-element simulation results, shown as *green dots*, even when the filling ratio is close to the tight-packing limit

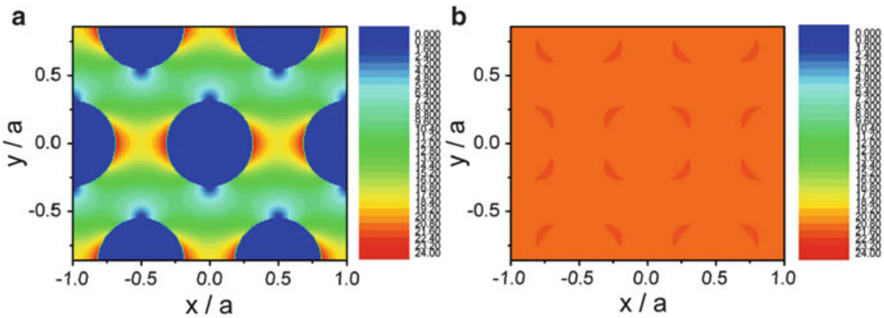

Fig. 5.28 (**a**) MST-calculated displacement field intensities in a 2D hexagonal lattice of Al cylinders in air, with the relevant experimental parameter values as stated in the text. *Blue* indicates low field intensity, and *yellow* indicates high field intensity. The wave vector is along the y-direction, with a being the lattice constant. It is seen that the wave amplitude is nearly zero inside the Al cylinders. Decreasing the frequency further does not alter this fact. (**b**) The same for PMMA cylinders in water. Wave field is seen to be much more homogeneous than that in (**a**). Figure adapted from [4]

5.6 Concluding Remarks

Acoustics has been one of the oldest topics of scientific investigation. Its robust revival during the past two decades has been a most gratifying experience for many researchers in this area. The purpose of this chapter is to give a vignette on some of the more recent developments. In particular, we present an overview on the different ramifications of the dynamic mass density issue that includes both the acoustic metamaterials manifestations and the effective mass density of fluid–solid composite in the zero frequency limit. The connection with the anti-resonance behavior is emphasized and clarified, especially with respect to the membrane-type acoustic metamaterials. A brief review of other types of acoustic metamaterials is also included.

In contrast to electromagnetic metamaterials, the role of dissipation is minimal for acoustic metamaterials—at least in the low-frequency limit. However, since the presence of dissipation is inevitable, its consideration, while still in the incipient stage at present, may become more important in the future. Another issue is the role of evanescent waves, which can be expected to play an increasingly important part in transformational acoustics, just as in the case of electromagnetic metamaterials. However, unlike the electromagnetic case, the elasticity of solid composites has more parameters and therefore can be expected to display a much richer variety of behaviors. An example along this direction is the recent work on hybrid elastic solids [79].

Potential applications of acoustic metamaterials would undoubtedly be a consideration for the future developments in this area. Pursuit of such a worthy goal may not only open up new topics for basic research, but can also impact those disciplines that are traditionally related to acoustics—such as architecture, noise pollution, medical ultrasound, acoustic imaging, etc. Cross-disciplinary pollination can imply exciting potential possibilities.

Acknowledgments Research works in dynamic mass density and membrane-type acoustic metamaterials have been supported by Hong Kong Research Grant Council grants HKUST6145/99P, HKUST6143/00P, HKUST 605405, and HKUST604207.

References

1. Z. Liu, X. Zhang, Y. Mao, Y.Y. Zhu, Z. Yang, C.T. Chan, P. Sheng, Locally resonant sonic materials. Science **289**, 1734 (2000). It should be noted that in this initial publication the metamaterial characteristic was mis-attributed to negative elastic modulus. This was subsequently corrected in Ref. 2
2. Z. Liu, C. Chan, P. Sheng, Analytical model of phononic crystal with local resonances. Phys. Rev. B **71**, 014103 (2005)
3. P. Sheng, X. Zhang, Z. Liu, C. Chan, Locally resonant sonic materials. Physica B Condens. Matter **338**, 201 (2003)
4. J. Mei, Z. Liu, W. Wen, P. Sheng, Effective mass density of fluid-solid composites. Phys. Rev. Lett. **96**, 24301 (2006)
5. J. Mei, Z. Liu, W. Wen, P. Sheng, Effective dynamic mass density of composites. Phys. Rev. B **76**, 134205 (2007)
6. Y. Wu, Y. Lai, Z.Q. Zhang, Effective medium theory for elastic metamaterials in two dimensions. Phys. Rev. B **76**, 205313 (2007)
7. G.W. Milton, J.R. Willis, On modifications of Newton's second law and linear continuum elastodynamics. Proc. R. Soc. A **463**, 855 (2007)

8. S. Yao, X. Zhou, G. Hu, Experimental study on negative effective mass in a 1d mass–spring system. New J. Phys. **10**, 043020 (2008)
9. D.L. Johnson, Equivalence between fourth sound in liquid He Ii at low temperatures and the Biot slow wave in consolidated porous media. Appl. Phys. Lett. **37**, 1065 (1980)
10. M.A. Biot, Theory of propagation of elastic waves in a fluid-saturated porous solid. I. Low-frequency range. J. Acoust. Soc. Am. **28**, 168 (1956)
11. T.J. Plona, Observation of a second bulk compressional wave in a porous medium at ultrasonic frequencies. Appl. Phys. Lett. **36**, 259 (1980)
12. P. Sheng, M.Y. Zhou, Dynamic permeability in porous media. Phys. Rev. Lett. **61**, 1591 (1988)
13. D. Weaire, Existence of a gap in the electronic density of states of a tetrahedrally bonded solid of arbitrary structure. Phys. Rev. Lett. **26**, 1541 (1971)
14. D.J. Ewins, *Modal Testing: Theory, Practice and Application* (Research Studies Press. Ltd., Hertfordshire, 2000)
15. M. Dilena, A. Morassi, The use of antiresonances for crack detection in beams. J. Sound Vib. **276**, 195 (2004)
16. M. Dilena, A. Morassi, Damage detection in discrete vibrating systems. J. Sound Vib. **289**, 830 (2006)
17. G. Schitter, K.J. Astrom, B.E. DeMartini, P.J. Thurner, K.L. Turner, P.K. Hansma, Design and modeling of a high-speed Afm-scanner. IEEE Trans. Control. Syst. Technol. **15**, 906 (2007)
18. G. Schitter, F. Allgöwer, A. Stemmer, A new control strategy for high-speed atomic force microscopy. Nanotechnology **15**, 108 (2004)
19. G. Schitter, P.J. Thurner, P.K. Hansma, Design and input-shaping control of a novel scanner for high-speed atomic force microscopy. Mechatronics **18**, 282 (2008)
20. Z. Yang, J. Mei, M. Yang, N. Chan, P. Sheng, Membrane-type acoustic metamaterial with negative dynamic mass. Phys. Rev. Lett. **101**, 204301 (2008)
21. S.H. Lee, C.M. Park, Y.M. Seo, Z.G. Wang, C.K. Kim, Acoustic metamaterial with negative density. Phys. Lett. A **373**, 4464 (2009)
22. S. Yao, X. Zhou, G. Hu, Investigation of the negative-mass behaviors occurring below a cut-off frequency. New J. Phys. **12**, 103025 (2010)
23. Z. Yang, H. Dai, N. Chan, G. Ma, P. Sheng, Acoustic metamaterial panels for sound attenuation in the 50–1000 Hz regime. Appl. Phys. Lett. **96**, 041906 (2010)
24. L. Landau, E. Lifshitz, *Theory of Elasticity*, 3rd edn. (Elmsford, New York, 1982)
25. J. Li, C. Chan, Double-negative acoustic metamaterial. Phys. Rev. E **70**, 055602 (2004)
26. Y. Ding, Z. Liu, C. Qiu, J. Shi, Metamaterial with simultaneously negative bulk modulus and mass density. Phys. Rev. Lett. **99**, 93904 (2007)
27. N. Fang, D. Xi, J. Xu, M. Ambati, W. Srituravanich, C. Sun, X. Zhang, Ultrasonic metamaterials with negative modulus. Nat. Mater. **5**, 452 (2006)
28. L. Fok, M. Ambati, X. Zhang, Acoustic metamaterials. MRS Bull. **33**, 931 (2008)
29. C. Ding, L. Hao, X. Zhao, Two-dimensional acoustic metamaterial with negative modulus. J. Appl. Phys. **108**, 074911 (2010)
30. C.L. Ding, X.P. Zhao, Multi-band and broadband acoustic metamaterial with resonant structures. J. Phys. D Appl. Phys. **44**, 215402 (2011)
31. S.H. Lee, C.M. Park, Y.M. Seo, Z.G. Wang, C.K. Kim, Acoustic metamaterial with negative modulus. J. Phys. Condens. Matter **21**, 175704 (2009)
32. C. Goffaux, J. Sánchez-Dehesa, A.L. Yeyati, P. Lambin, A. Khelif, J. Vasseur, B. Djafari-Rouhani, Evidence of fano-like interference phenomena in locally resonant materials. Phys. Rev. Lett. **88**, 225502 (2002)
33. Y. Cheng, J. Xu, X. Liu, One-dimensional structured ultrasonic metamaterials with simultaneously negative dynamic density and modulus. Phys. Rev. B **77**, 045134 (2008)
34. X. Hu, K.M. Ho, C. Chan, J. Zi, Homogenization of acoustic metamaterials of Helmholtz resonators in fluid. Phys. Rev. B **77**, 172301 (2008)

35. S.H. Lee, C.M. Park, Y.M. Seo, Z.G. Wang, C.K. Kim, Composite acoustic medium with simultaneously negative density and modulus. Phys. Rev. Lett. **104**, 54301 (2010)
36. S.H. Lee, C.M. Park, Y.M. Seo, C.K. Kim, Reversed Doppler effect in double negative metamaterials. Phys. Rev. B **81**, 241102 (2010)
37. M. Ambati, N. Fang, C. Sun, X. Zhang, Surface resonant states and superlensing in acoustic metamaterials. Phys. Rev. B **75**, 195447 (2007)
38. S. Guenneau, A. Movchan, G. Pétursson, S. Anantha Ramakrishna, Acoustic metamaterials for sound focusing and confinement. New J. Phys. **9**, 399 (2007)
39. K. Deng, Y. Ding, Z. He, H. Zhao, J. Shi, Z. Liu, Theoretical study of subwavelength imaging by acoustic metamaterial slabs. J. Appl. Phys. **105**, 124909 (2009)
40. X. Zhou, G. Hu, Superlensing effect of an anisotropic metamaterial slab with near-zero dynamic mass. Appl. Phys. Lett. **98**, 263510 (2011)
41. J. Li, Z. Liu, C. Qiu, Negative refraction imaging of acoustic waves by a two-dimensional three-component phononic crystal. Phys. Rev. B **73**, 054302 (2006)
42. S. Zhang, L. Yin, N. Fang, Focusing ultrasound with an acoustic metamaterial network. Phys. Rev. Lett. **102**, 194301 (2009)
43. L. Zigoneanu, B.I. Popa, S.A. Cummer, Design and measurements of a broadband two-dimensional acoustic lens. Phys. Rev. B **84**, 024305 (2011)
44. P.A. Belov, C.R. Simovski, P. Ikonen, Canalization of subwavelength images by electromagnetic crystals. Phys. Rev. B **71**, 193105 (2005)
45. Y. Jin, S. He, Canalization for subwavelength focusing by a slab of dielectric photonic crystal. Phys. Rev. B **75**, 195126 (2007)
46. Z. He, F. Cai, Y. Ding, Z. Liu, Subwavelength imaging of acoustic waves by a canalization mechanism in a two-dimensional phononic crystal. Appl. Phys. Lett. **93**, 233503 (2008)
47. X. Ao, C. Chan, Far-field image magnification for acoustic waves using anisotropic acoustic metamaterials. Phys. Rev. E **77**, 025601 (2008)
48. Z. Jacob, L.V. Alekseyev, E. Narimanov, Optical hyperlens: far-field imaging beyond the diffraction limit. Opt. Express **14**, 8247 (2006)
49. Z. Liu, H. Lee, Y. Xiong, C. Sun, X. Zhang, Far-field optical hyperlens magnifying sub-diffraction-limited objects. Science **315**, 1686 (2007)
50. D. Smith, D. Schurig, Electromagnetic wave propagation in media with indefinite permittivity and permeability tensors. Phys. Rev. Lett. **90**, 77405 (2003)
51. J. Li, L. Fok, X. Yin, G. Bartal, X. Zhang, Experimental demonstration of an acoustic magnifying hyperlens. Nat. Mater. **8**, 931 (2009)
52. F. Liu, F. Cai, S. Peng, R. Hao, M. Ke, Z. Liu, Parallel acoustic near-field microscope: a steel slab with a periodic array of slits. Phys. Rev. E **80**, 026603 (2009)
53. J. Zhu, J. Christensen, J. Jung, L. Martin-Moreno, X. Yin, L. Fok, X. Zhang, F. Garcia-Vidal, A holey-structured metamaterial for acoustic deep-subwavelength imaging. Nat. Phys. **7**, 52 (2010)
54. A. Spadoni, C. Daraio, Generation and control of sound bullets with a nonlinear acoustic lens. Proc. Natl. Acad. Sci. **107**, 7230 (2010)
55. G.W. Milton, M. Briane, J.R. Willis, On cloaking for elasticity and physical equations with a transformation invariant form. New J. Phys. **8**, 248 (2006)
56. H. Chen, C. Chan, Acoustic cloaking in three dimensions using acoustic metamaterials. Appl. Phys. Lett. **91**, 183518 (2007)
57. S.A. Cummer, D. Schurig, One path to acoustic cloaking. New J. Phys. **9**, 45 (2007)
58. Y. Cheng, F. Yang, J.Y. Xu, X.J. Liu, A multilayer structured acoustic cloak with homogeneous isotropic materials. Appl. Phys. Lett. **92**, 151913 (2008)
59. J. Pendry, J. Li, An acoustic metafluid: realizing a broadband acoustic cloak. New J. Phys. **10**, 115032 (2008)
60. D. Torrent, J. Sánchez-Dehesa, Acoustic cloaking in two dimensions: a feasible approach. New J. Phys. **10**, 063015 (2008)

61. S.A. Cummer, B.I. Popa, D. Schurig, D.R. Smith, J. Pendry, M. Rahm, A. Starr, Scattering theory derivation of a 3d acoustic cloaking shell. Phys. Rev. Lett. **100**, 24301 (2008)
62. A.N. Norris, Acoustic cloaking theory. Proc. R. Soc. A **464**, 2411 (2008)
63. Y. Urzhumov, F. Ghezzo, J. Hunt, D.R. Smith, Acoustic cloaking transformations from attainable material properties. New J. Phys. **12**, 073014 (2010)
64. Y. Bobrovnitskii, Impedance acoustic cloaking. New J. Phys. **12**, 043049 (2010)
65. Z. Liang, J. Li, Bending a periodically layered structure for transformation acoustics. Appl. Phys. Lett. **98**, 241914 (2011)
66. X. Zhu, B. Liang, W. Kan, X. Zou, J. Cheng, Acoustic cloaking by a superlens with single-negative materials. Phys. Rev. Lett. **106**, 14301 (2011)
67. H. Chen, C. Chan, Acoustic cloaking and transformation acoustics. J. Phys. D Appl. Phys. **43**, 113001 (2010)
68. M. Farhat, S. Enoch, S. Guenneau, A. Movchan, Broadband cylindrical acoustic cloak for linear surface waves in a fluid. Phys. Rev. Lett. **101**, 134501 (2008)
69. M. Farhat, S. Guenneau, S. Enoch, A.B.. Movchan, Cloaking bending waves propagating in thin elastic plates. Phys. Rev. B **79**, 033102 (2009)
70. M. Farhat, S. Guenneau, S. Enoch, Ultrabroadband elastic cloaking in thin plates. Phys. Rev. Lett. **103**, 24301 (2009)
71. A. Norris, A. Shuvalov, Elastic cloaking theory. Wave Motion **48**, 525–538 (2011)
72. Y.A. Urzhumov, D.R. Smith, Fluid flow control with transformation media. Phys. Rev. Lett. **107**, 074501 (2011)
73. S. Zhang, C. Xia, N. Fang, Broadband acoustic cloak for ultrasound waves. Phys. Rev. Lett. **106**, 24301 (2011)
74. B.I. Popa, L. Zigoneanu, S.A. Cummer, Experimental acoustic ground cloak in air. Phys. Rev. Lett. **106**, 253901 (2011)
75. B. Liang, B. Yuan, J. Cheng, Acoustic diode: rectification of acoustic energy flux in one-dimensional systems. Phys. Rev. Lett. **103**, 104301 (2009)
76. B. Liang, X. Guo, J. Tu, D. Zhang, J. Cheng, An acoustic rectifier. Nat. Mater. **9**, 989 (2010)
77. N. Boechler, G. Theocharis, C. Daraio, Bifurcation-based acoustic switching and rectification. Nat. Mater. **10**, 665 (2011)
78. X.F. Li, X. Ni, L. Feng, M.H. Lu, C. He, Y.F. Chen, Tunable unidirectional sound propagation through a sonic-crystal-based acoustic diode. Phys. Rev. Lett. **106**, 84301 (2011)
79. Y. Lai, Y. Wu, P. Sheng, Z.Q. Zhang. Hybrid elastic solids. Nat. Mater. **10**, 620 (2011)
80. J. Mei, Z. Liu, J. Shi, D. Tian, Theory for elastic wave scattering by a two-dimensional periodical array of cylinders: an ideal approach for band-structure calculations. Phys. Rev. B **67**, 245107 (2003)
81. J. Mei, Z. Liu, C. Qiu, Multiple-scattering theory for out-of-plane propagation of elastic waves in two-dimensional phononic crystals. J. Phys. Condens. Matter **17**, 3735 (2005)
82. P. Sheng, *Introduction to Wave Scattering, Localization and Mesoscopic Phenomena*, vol. 88, Springer Series in Materials Science (Springer, 2006)
83. J.G. Berryman, Long wavelength propagation in composite elastic media I. Spherical inclusions. J. Acoust. Soc. Am. **68**, 1809 (1980)
84. L.M. Schwartz, D.L. Johnson, Long-wavelength acoustic propagation in ordered and disordered suspensions. Phys. Rev. B **30**, 4302 (1984)
85. R. Lakes, T. Lee, A. Bersie, Y. Wang, Extreme damping in composite materials with negative-stiffness inclusions. Nature **410**, 565 (2001)
86. F. Cervera, L. Sanchis, J. Sanchez-Perez, R. Martinez-Sala, C. Rubio, F. Meseguer, C. Lopez, D. Caballero, J. Sanchez-Dehesa, Refractive acoustic devices for airborne sound. Phys. Rev. Lett. **88**, 23902 (2001)
87. J. Mei, Y. Wu, Z. Liu, Effective medium of periodic fluid-solid composites, Eur. Phys. Lett. **98**, 54001 (2012)